Particles, Drops, and Bubbles Moving Across Sharp Interfaces and Stratified Layers

— Source link ↗

Jacques Magnaudet, Matthieu Mercier

Institutions: Massachusetts Institute of Technology

Topics: Stratified flows and Particle-laden flows

Related papers:

- Enhanced drag of a sphere settling in a stratified fluid at small Reynolds numbers

- Prolonged residence times for particles settling through stratified miscible fluids in the Stokes regime

- Gravitational settling of particles through density interfaces

- Core mechanisms of drag enhancement on bodies settling in a stratified fluid

- Inertial drag on a sphere settling in a stratified fluid

This is an author's version published in: http://oatao.univ-toulouse.fr/24553

Particles, Drops, and Bubbles Moving Across Sharp Interfaces and Stratified Layers

Jacques Magnaudet and Matthieu J. Mercier

Institut de Mécanique des Fluides de Toulouse (IMFT), CNRS UMR 5502, Université de Toulouse, 31400 Toulouse, France; email: Jacques.Magnaudet@imft.fr, Matthieu.Mercier@imft.fr

Keywords

stratified flows, multiphase flows, particle-laden flows, drops and bubbles, interfacial flows, drift volume

Abstract

Rigid or deformable bodies moving through continuously stratified layers or across sharp interfaces are involved in a wide variety of geophysical and engineering applications, with both miscible and immiscible fluids. In most cases, the body moves while pulling a column of fluid, in which density and possibly viscosity differ from those of the neighboring fluid. The presence of this column usually increases the fluid resistance to the relative body motion, frequently slowing down its settling or rise in a dramatic manner. This column also exhibits specific dynamics that depend on the nature of the fluids and on the various physical parameters of the system, especially the strength of the density/viscosity stratification and the relative magnitude of inertia and viscous effects. In the miscible case, as stratification increases, the wake becomes dominated by the presence of a downstream jet, which may undergo a specific instability. In immiscible fluids, the viscosity contrast combined with capillary effects may lead to strikingly different evolutions of the column, including pinch-off followed by the formation of a drop that remains attached to the body, or a massive fragmentation phenomenon. This review discusses the flow organization and its consequences on the body motion under a wide range of conditions, as well as potentialities and limitations of available models aimed at predicting the body and column dynamics.

1. INTRODUCTION

Rigid or deformable bodies that settle or rise through steeply or continuously stratified fluid layers are encountered in an extremely wide range of fields, from astrophysics and geophysics to engineering and microfluidics applications.

In astrophysics, buoyant bubbles of relativistic plasma rising in the stratified atmosphere of galaxy cluster cores are suspected to be an efficient vehicle for transferring energy from massive black holes to the intracluster medium (Zhang et al. 2018). In oceanography, plankton and marine snow drifting in oceans and estuaries face a surrounding fluid medium locally comprising large density gradients due to the presence of thermoclines and haloclines. It is now established that the corresponding discontinuities or inhomogeneous layers modify, often dramatically, the settling rate and horizontal dispersion characteristics of inert particles and living microorganisms (Lande & Wood 1987, Riebesell 1992, Denman & Gargett 1995, MacIntyre et al. 1995, Allredge et al. 2002). This conclusion extends to configurations encountered in the context of ocean engineering, such as the drift of Lagrangian buoys (D'Asaro 2003) or the rising time of oil droplets resulting from deepwater oil spills (Dietrich et al. 2014). Similarly, inversion layers in the troposphere affect the fate of pollutants, pollens, dust, or volcanic ashes (King et al. 1987, Chemel & Burns 2015). In both contexts, stable stratification may deeply influence the dispersion, survival, or growth of colonizing populations of small living organisms (Condie & Bormans 1997, Widder et al. 1999, Bearon & Grünbaum 2006, Doostmohammadi et al. 2012). These various consequences of density stratification at the particle scale make the underlying fluid mechanical processes of primary importance to better understand air and marine pollution, possible biogenic mixing in oceans, and on larger timescales, climate variability and biogeochemical cycles.

Fluids involved in internal geophysical processes comprise compositional discontinuities resulting in sharp density and viscosity gradients. The mixing of acid and basic magmas is often considered to trigger explosive volcanic eruptions, such as the 1875 Plinian eruption of Askja in Iceland (Sparks et al. 1977). The settling of solid crystals across the interface separating the two compositionally different magmas was recently suggested to be one of the important mechanisms capable of achieving this mixing (Renggli et al. 2016). Plumes ascending through the Earth's mantle behave as buoyant low-viscosity fluid regions compared to the carrying medium (Steinberger & O'Connell 1998, Kumagai et al. 2007). The carrying medium is discontinuous at several locations, especially at the boundary between the lower and the upper mantle, and between the upper mantle and the crust. These discontinuities modify the shape of the plumes through variations of stresses at their surface, which in turn change the amount of material exchanged between adjacent layers (Manga et al. 1993).

Most engineering applications in which rigid or fluid particles cross an interface involve immiscible liquids. In this context, effects of interfacial tension or viscosity contrast generally play a leading role. Encapsulation and coating processes often use gravity (Kawano et al. 1996, Pitois et al. 1999) or, for micrometer-size objects, magnetic forces (Tsai et al. 2011, Sinha et al. 2013) to drive particles across an interface so as to coat them with one of the fluids while they penetrate into the other. In the final stages of liquid–liquid extraction, one of the most widely used chemical engineering processes (Rydberg et al. 2004), a layer of liquid A stands on top of a bath of a heavier liquid B, and droplets of A rising into B eventually cross the A/B horizontal interface and coalesce with the top layer, while droplets of B settling into A follow a similar route in the opposite direction. In the ladle stirring technique routinely employed in steel elaboration, nonmetallic impurities are transferred from liquid metal to slag with the help of gas bubbles (Poggi et al. 1969, Reiter & Schwerdtfeger 1992, Kobayashi 1993, Han & Holappa 2008). Some scenarios of nuclear accidents involve the ablation of the concrete slab below the reactor by the fuel-containing

material (corium), which in turn generates gas bubbles that later cross the interface separating the metallic an oxide layers of the corium (Sehgal 2012, Jacquemain 2015).

One crucial link between all the aforementioned situations is that—provided they succeed in crossing isopycnals or sharp interfaces—particles, microorganisms, drops, or bubbles drag a certain amount of fluid that takes the form of a column (or tail) within which the local physical properties differ from those of the fluid located beside and ahead of the body. This tail affects the overall fluid resistance to the body motion and may, under certain circumstances, dramatically affect its settling or rise. Moreover, its dynamics change quantitatively and qualitatively with the control parameters, and specific instabilities can develop within it or at its surface. These features may also affect the body motion in various ways.

These are the main phenomena to be discussed in this review. The focus is deliberately on mechanisms at the particle scale, although collective effects are also of primary importance to understand the behavior of particle clusters (Noh 2000, Bush et al. 2003), the evolution of inert or active suspensions in continuously stratified environments [Blanchette & Bush (2005), Bearon et al. (2006), Blanchette (2013), Wagner et al. (2014), Ardekani et al. (2017) and references therein], or the dynamics of interacting particles, drops, and bubbles standing at sharp interfaces (Cooray et al. 2017) or moving in their vicinity (Manga & Stone 1995). Much progress has been achieved over the last two decades in the description of stratification-induced phenomena at the local scale, especially thanks to advanced imaging and computational techniques, and this review is largely built on the corresponding material. Section 2 discusses two fundamental aspects that serve as a reference and help understand some of the key features encountered in most flow situations under consideration. Section 3 provides an overview of the specificities of the flow fields past bodies settling or rising in a continuously stably stratified fluid, with an emphasis on the wake structure and consequences for the body drag. Section 4 focuses on the case of immiscible fluids in which effects of viscosity, density contrasts, and interfacial tension play a major role on the conditions allowing bodies to cross the interface, on the short- and long-term evolutions of the tail, and on the body dynamics during the entire breakthrough.

2. GENERAL CONCEPTS

2.1. Vorticity Generation in Inhomogeneous Fluids

In all situations considered here, vorticity is generated in the bulk or at interfaces by gradients or jumps of physical or geometrical properties, including density ρ, viscosity μ, possibly interfacial tension γ, and interface curvature $\kappa = \nabla \cdot \mathbf{n}$, where $\mathbf{n}$ is the local unit normal to the considered interface. We restrict the discussion to Newtonian fluids, incompressible flows, and conservative body forces. Under such conditions, considering the velocity $\mathbf{u}$, pressure p, and physical properties as generalized functions of time and position throughout the fluid domain, the governing equation for the vorticity $\boldsymbol{\omega} = \nabla \times \mathbf{u}$ may be written as

$$\frac{D\boldsymbol{\omega}}{Dt} = \boldsymbol{\omega} \cdot \nabla \mathbf{u} - \nabla \times \left(\frac{\mu}{\rho} \nabla \times \boldsymbol{\omega} \right) + \underbrace{\frac{\nabla \rho}{\rho^2} \times \nabla p}_{(1)} + \underbrace{2 \nabla \times \left(\frac{\nabla \mu}{\rho} \cdot \mathbb{S} \right)}_{(2)} - \underbrace{\nabla \left(\frac{\gamma}{\rho} \kappa \right) \times \mathbf{n} \delta_\mathrm{s}}_{(3)}, \quad 1.$$

where D/Dt is the material derivative, $\mathbb{S} = \frac{1}{2}(\nabla \mathbf{u} + \nabla \mathbf{u}^\mathrm{T})$ is the strain rate tensor, and δ_s is the surface delta function, which is nonzero only at interfaces.

Here we are interested in situations where vorticity is generated within the fluid domain through at least one of the last three terms in the right-hand side of Equation 1. Once advected and diffused within the flow, this free vorticity interacts nonlinearly with its bound counterpart

generated at the body surface by the corresponding boundary condition, which ranges from no-slip for rigid bodies to shear-free for clean (i.e., surfactant-free) bubbles with negligible inner viscosity. Term 1 in the above equation, the so-called baroclinic torque due to a misalignment between the pressure and density gradients, is the most familiar one, being the only one involved in density-stratified fluids with uniform viscosity, which are ubiquitous in geophysical flows. Term 2 is known to be important in compressible flows (Hokenson 1986), as well as in continuously viscosity-stratified flows in which stratification arises from compositional variations, such as oil reservoirs. It is also responsible for vorticity generation at interfaces between immiscible fluids with different viscosities, through the action of interfacial shear and normal strain. Density and viscosity jumps being normal to interfaces, term 2 may comprise a baroclinic contribution, $-2\rho^{-2}\nabla\rho \times (\nabla\mu \cdot \mathbb{S})$, when the density jump and the interfacial shear are both nonzero. Term 3 is specific to immiscible fluids and generates tangential vorticity at interfaces through variations of their curvature and possible surface tension gradients or jumps responsible for the Marangoni effect (Levich & Krylov 1969).

## 2.2. Fluid Entrainment and Drift Volume

Whatever the flow regime, a translating body displaces a certain amount of fluid. This volume, frequently termed the drift volume, may be rigorously defined by considering fluid particles initially standing at position $\mathbf{x_0} = (x_0, y_0, z_0)$ within the plane $x = x_0$ located far ahead of the body (which stands initially at $x = 0$) and perpendicular to its motion. After the body has moved an infinite distance forward, these fluid particles eventually reach the longitudinal position $X(y_0, z_0) = \lim_{t\to\infty} \mathbf{x}(\mathbf{x_0}) \cdot \mathbf{e_x} = x_0 + \int_0^\infty \mathbf{u}[\mathbf{x}(t)] \cdot \mathbf{e_x}\,dt$, with $\mathbf{e_x}$ the unit vector in the x-direction. The drift volume enclosed within the plane $x = x_0$ and the envelope of all final positions X is then

$$\mathcal{V}_D = \int_{-\infty}^{+\infty} \int_{-\infty}^{+\infty} [X(y_0, z_0) - x_0]\,dydz \qquad 2.$$

Darwin (1953) determined the path lines of fluid particles past a circular cylinder and a sphere with radius a translating in a homogeneous fluid and under potential flow conditions. He established that in both cases the ratio of the drift volume to the body volume, $\mathcal{V}$, equals the translational added-mass coefficient, C_M (with $C_M = 1$ and $1/2$ for a cylinder and a sphere, respectively). The result generalizes to arbitrary body shapes. Nevertheless, due to the conditionally convergent integrals involved, it is influenced by the order in which integrations are performed (Darwin 1953) and by the ratio of the initial body-to-plane distance, x_0, to the maximum initial radial position of the considered fluid particles, $\mathfrak{h}_M = \text{Max}(\mathfrak{h}_0)$, with $\mathfrak{h}_0 = (y_0^2 + z_0^2)^{1/2}$ (Benjamin 1986). Actually, the equality $\mathcal{V}_D = C_M\mathcal{V}$ only holds in the limits of $x_0 \to \infty$, $\mathfrak{h}_M/a \to \infty$, and $\mathfrak{h}_M/x_0 \to 0$ (Eames et al. 1994).

Under these conditions, the direct connection between the drift volume and the virtual (or added) mass associated with a translating body, be it a rigid object or a well-defined body of fluid such as a vortex (Dabiri 2006), makes the determination of $\mathcal{V}_D$ useful to indirectly evaluate the hydrodynamic force acting on accelerating bodies, including contributions from the fluid displaced by wake vortices. The concept is, for instance, useful in the case of arrays of particles, drops, and bubbles (Eames 2003), as well as swimming animals (Dabiri 2005). It may also be used to estimate the amount of light fluid entrained by bodies settling in a stratified two-layer miscible fluid setup (Camassa et al. 2008).

The definition in Equation 2 above is valid whether or not viscous effects take place. The drift volume past a spherical drop translating in a homogeneous fluid under Stokes flow conditions
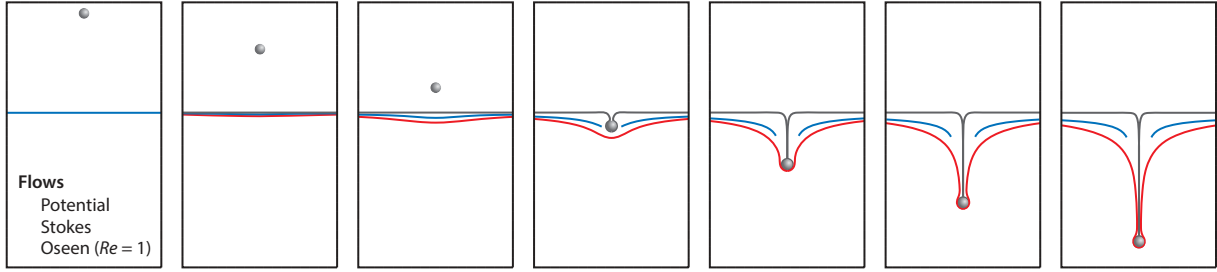
Figure 1

The partial drift volume induced by the uniform translation of a sphere of radius a under various flow conditions ($x_0/a = 18$ and $\mathfrak{h}_M/a = 14$, where $\mathfrak{h}_M$ is the maximum initial radial position of the considered fluid particles). Black, red, and blue lines refer to potential, Stokes, and Oseen flows, respectively, with a Reynolds number (Re) of 1 in the latter case. Close to the vertical centerline, the blue line is not shown after the sphere has crossed the marked plane because the Oseen solution is not valid in the sphere vicinity. Figure adapted from an original courtesy of J.L. Pierson.

was considered by Eames et al. (2003). In this case, due to the r^{-1} decay of $\mathbf{u}$ (with r the distance to the body center), $\mathcal{V}_D$ is unbounded and only the partial drift volume corresponding to a finite body displacement and finite x_0 and $\mathfrak{h}_M$ may be properly defined. This is because the streamlines associated with the Stokeslet solution are open, making all fluid particles move forward irrespective of their initial radial position (i.e., there is no reflux), in contrast with the closed-streamline structure associated with the potential dipole in the inviscid case (**Figure 1**). A partial drift volume may also be computed in wall-bounded domains since the screening effect induced by the vanishing of the normal component of the velocity disturbance at the wall makes it decay as r^{-2} (r^{-3}) when the body moves parallel (perpendicular) to the wall. In particular, if the material particles stand initially in a plane parallel to a wall and lying a large distance $h \gg a$ from it, $\mathcal{V}_D(h/a)$ is of order $\mathcal{O}[(h/a)^2\mathcal{V}]$, hence much larger than the body volume. The influence of finite inertia may be appreciated by considering the Oseen approximation, which is valid for small but finite body Reynolds number, $Re = \rho V a/\mu \ll 1$, where V is the body velocity. Under such conditions, inertia dominates outside the $\mathcal{O}(aRe^{-1})$-large Stokes region and the viscous wake whose radius at position x varies as $a(Vt - x)Re^{-1/2}$ (Batchelor 1967). Since these two regions, where $\mathbf{u}$ decays as $\mathcal{O}(r^{-1})$, decrease in size as Re increases, so does the entrained volume. This conclusion extends to flows with higher Re, in which most entrainment takes place in the wake. Nevertheless, all particles with radial positions $\mathfrak{h}_0 \leq \mathfrak{h}_M$ in the plane $x = x_0$ eventually stand within the wake when $(Vt - x_0)/a$ is approximately greater than $Re(\mathfrak{h}_M/a)^2$, making the partial drift volume $\mathcal{V}_D(\mathfrak{h}_M, x_0, t)$ diverge with $t \to \infty$, however large Re may be (Chisholm & Khair 2017).

3. BODIES MOVING ALONG A CONTINUOUS DENSITY PROFILE

3.1. Flow Structure

Provided density variations are small enough for the Boussinesq approximation to hold, effects of stratification in a fluid with a continuous vertical density distribution are characterized by the Brunt–Väisälä frequency, $N = (-\frac{g}{\rho_0}\rho_z)^{1/2}$, where ρ_0 is the reference density, $\rho_z < 0$ is the stabilizing background density gradient, and g is gravity. The dynamics of a body with characteristic length scale a settling or rising with speed V in such a fluid are then governed by three characteristic parameters. In addition to the Reynolds number, $Re = aV/\nu$, where $\nu = \mu/\rho_0$ is the kinematic viscosity, these dynamics depend on the Froude number, $Fr = V/Na$, which compares buoyancy and inertial forces, and on the Prandtl number comparing momentum and

density diffusion, $Pr = \nu/\kappa$, where κ is the molecular diffusivity of the stratifying agent (viscosity stratification is not considered in this section).

A combination of experiments in the range $10^2 \lesssim Re \lesssim 1.5 \times 10^3$ and numerical simulations with $Re \lesssim 200$ gradually revealed the specific structure of the flow past a sphere towed through a linearly stratified fluid layer, especially the radiated internal waves pattern (Mowbray & Rarity 1967), the gradual shrinking of the toroidal attached eddy as Fr decreases (Torres et al. 2000), and the existence of a thin upward jet that dominates the wake structure for $Fr \lesssim 1$ (Torres et al. 2000, Hanazaki et al. 2009a).

Compared to the homogeneous case ($Fr = \infty$), finite-Fr effects lead to many different flow regimes because stratification introduces a specific length scale, ℓ_s, which in general depends on Fr, Re, and Pr and competes with scales involved in the unstratified case (Zhang et al. 2019). In particular, stratification tends to inhibit vertical motions in the flow past the body at scales of the order of ℓ_s, whatever the value of Re. This is especially clear for $Re = 0$, where the flow structure corresponding to the Stokes problem in a linearly stratified fluid is intrinsically different from the classical structure corresponding to the Stokeslet solution (**Figure 2a**). In this case, we have $\ell_s = (\nu\kappa/N^2)^{1/4}$, and the resulting Stratlet fundamental solution induces toroidal eddies centered on the sphere, with a typical vertical extent of ℓ_s (Ardekani & Stocker 2010). With low but finite Reynolds numbers (**Figure 2b**), the structure of the Stokeslet solution is still dominant for large-enough Fr, although isopycnals are distorted and entrained downward by the passing sphere. Toroidal eddies similar to those predicted by the Stratlet solution are present whatever the value of Fr, with an extent that becomes of the order of the sphere size for $\mathcal{O}(1)$ Froude numbers. Compared to the zero-Re solution, the approximate fore–aft symmetry of the velocity field disappears for such Fr, and a flow region with significant upward velocities occurs at the rear of the sphere. This specific structure is driven by the baroclinic torque in Equation 1, which converts the positive radial density gradient resulting from the deflection of the isopycnals into positive azimuthal vorticity, i.e., upward velocities near the flow axis. This inertial mechanism is generic: A downstream jet is also predicted in the case of a body translating parallel to the density gradient in an inviscid variable-density fluid in which density changes modify the inertia term in the momentum (Euler) equation but do not induce a buoyancy force (Eames & Hunt 1997).

Several distinct wake structures, labeled as regimes A–G in **Figure 2c**, have been identified in the ranges of $10 \le Re \lesssim 1.5 \times 10^3$ and $0.2 \le Fr \le 50$, with $Pr \approx 700$ (Hanazaki et al. 2009a), some of which have been specifically investigated numerically [regimes A, B, and D (Torres et al. 2000, Hanazaki et al. 2009b, Yick et al. 2009)] or experimentally [regimes A and B (Okino et al. 2017)]. In the latter, the far-field dynamics are dominated by internal lee waves adequately described by the linear theory of Mowbray & Rarity (1967) (**Figure 2d** and **Figure 3c–e**), while the near wake is dominated by an intense upward jet, which is the sequel of the upward velocity region observed at low but finite Re. A conspicuous bell-shape structure (Hanazaki et al. 2009a, Hanazaki 2015, Okino et al. 2017) takes place at some distance from the sphere (scaling as Fr) in this jet (**Figure 3a**), in the region where downward velocities around the jet are maximum (**Figure 3c–d**).

As Fr decreases and Re is of $\mathcal{O}(10^2)$, a wake instability manifests itself, either through a flapping of the bell-shape structure (**Figure 3a,b**) or by creating knots in the density field, without any vortex shedding (regimes A and D). With $Re > 20$, the jet radius and the maximum density/velocity disturbance along the jet axis respectively scale as $(Fr/Re)^{1/2}$ and $Fr^{-1/2}$ near the sphere, while the jet extends over a vertical distance, scaling as Fr (**Figure 3c–e**) (Hanazaki 2015, Okino et al. 2017). In contrast, with $Re < 10$, the jet radius and vertical extent scale as $(Fr^2/Re)^{1/3}$ and $Fr^{1/2}$, respectively (Yick et al. 2009). Whatever the value of Re, the higher Pr is, the thinner the jet and the larger the maximum upward velocity on the jet axis, other things equal (Hanazaki et al. 2009b, Yick et al. 2009, Zhang et al. 2019). The jet weakens as the Froude number increases, and the usual
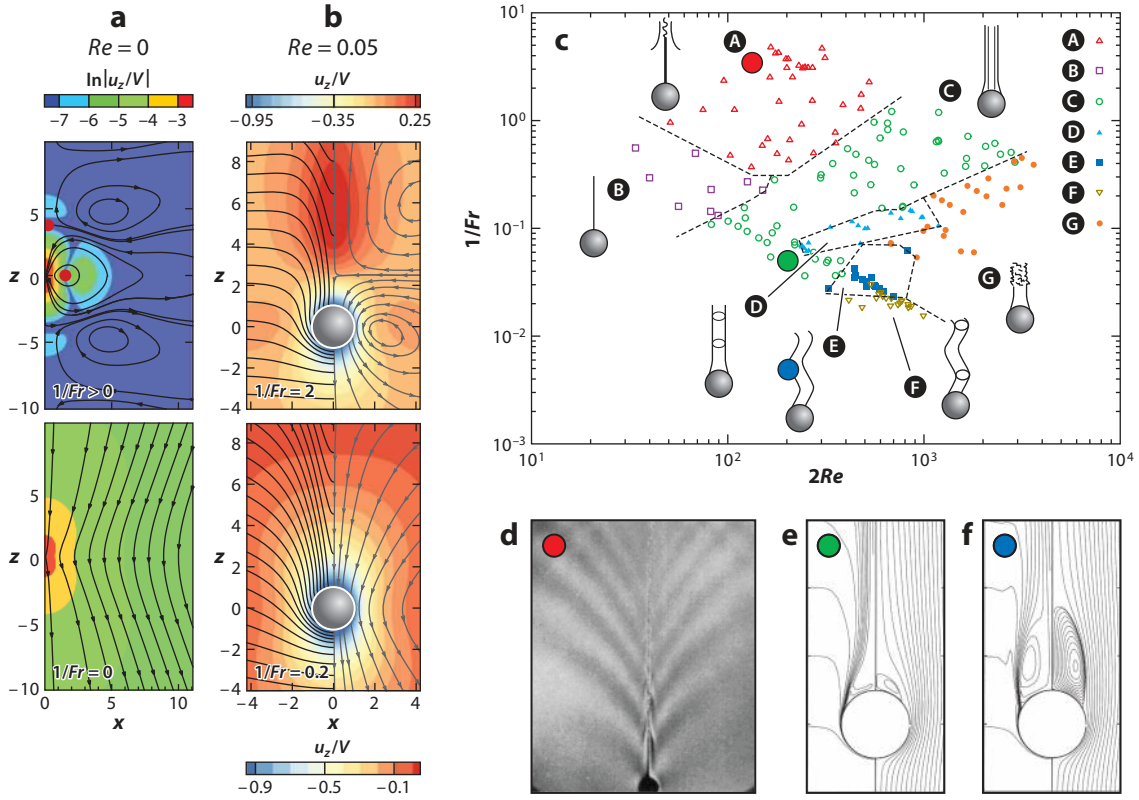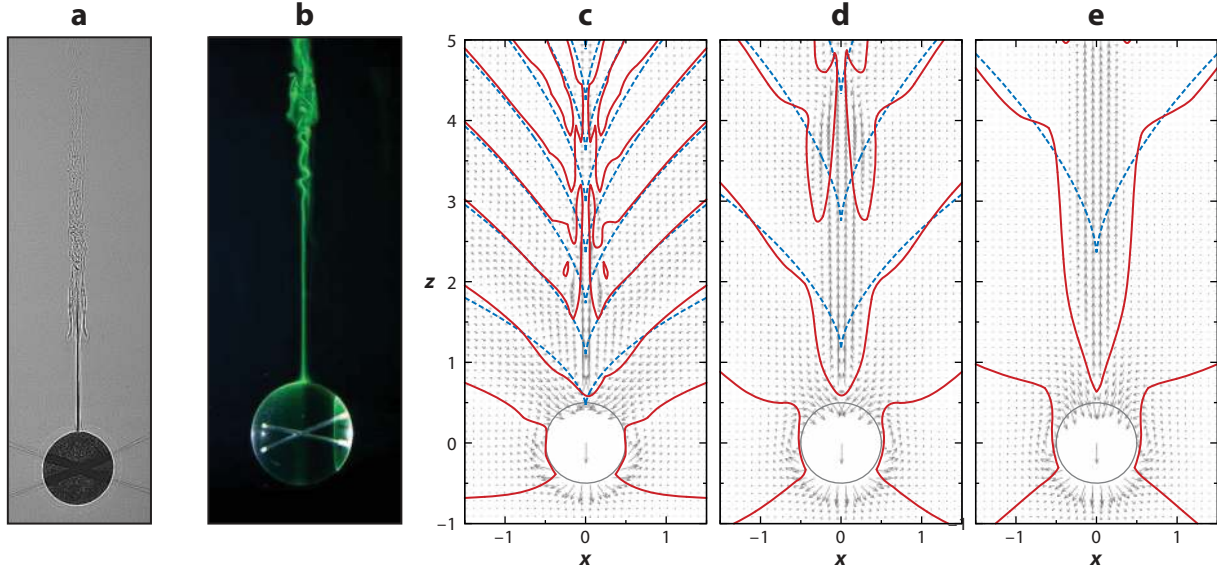
Figure 2

Flow regimes past a sphere settling in a linearly stratified fluid. (*a*) Vertical velocity iso-levels and streamlines in the zero–Reynolds number (*Re*) flow induced by the Stratlet solution (*top*) and the Stokeslet solution (*bottom*). (*b*) Low-but-finite-*Re* flow structure at $Re = 0.05$ ($Pr = 700$), for Froude numbers (*Fr*) 0.5 (*top*) and 5 (*bottom*), with vertical velocity iso-levels in the laboratory frame, isopycnals (*left half*), and streamlines (*right half*). In panels *a* and *b*, coordinates are normalized by the specific length scale, $\ell_s = (\nu\kappa/N^2)^{1/4}$, and the sphere radius, *a*, respectively, where ν is the kinematic viscosity, κ is the molecular diffusivity of the stratifying agent, and *N* is the Brunt–Väisälä frequency. The vertical fluid velocity u_z is normalized by the sphere settling velocity *V*. (*c*) Wake structure map as a function of *Re* and Fr^{-1}. (*d*) Shadowgraph image of the internal lee waves in regime A of panel *c*. (*e,f*) Isopycnals (*left half*) and streamlines (*right half*) for $Re = 100$, with (*e*) $Fr = 20$ and (*f*) $Fr = 200$. Panels adapted from (*a*) Ardekani & Stocker (2010), (*b*) Zhang et al. (2019), (*c*) Hanazaki et al. (2009a), (*d*) Mowbray & Rarity (1967), and (*e,f*) Torres et al. (2000), with permission from (*a,b*) American Physical Society and (*c–f*) Cambridge University Press.

axisymmetric wake structure with a toroidal standing eddy, observed in a homogeneous fluid for $10 \lesssim Re \lesssim 105$, is gradually recovered beyond $Fr \approx 20$ (**Figure 2e–f**) (Torres et al. 2000, Zhang et al. 2019). The higher *Pr* is, the stronger the shrinking of the toroidal eddy at a given (*Re*, *Fr*) (Hanazaki et al. 2009b).

3.2. Buoyancy-Induced Drag Increase and Body Dynamics

Isopycnals' distortion due to the body translation modifies the surrounding flow field, yielding an additional vertical net force, which in turn affects the body dynamics. In the inviscid limit, assuming $a|\rho_z|/\rho_0 \ll 1$ and evaluating the alteration of the inertial term in the Euler equation by the density disturbance in the absence of any buoyancy effect, Eames & Hunt (1997) found this force to be $F_s = -\frac{1}{2}C_M\mathcal{V}\rho_z V^2$, for both a sphere and a circular cylinder with a horizontal

Figure 3

Wake structure past a settling sphere for Reynolds number (Re) of $\mathcal{O}(10^2)$ and Froude number (Fr) of $\mathcal{O}(1)$ or less. (*a*) Shadowgraph image ($Re = 100$) and (*b*) fluorescent dye visualization ($Re = 115$) of the rear jet in regime A from **Figure 2** at $Fr = 0.3$. (*c*–*e*) Velocity field from numerical simulations in regime B from **Figure 2** ($Re = 112$), with $Fr = 0.4$, 1.0, and 2.0, respectively. Solid and dashed lines represent zero–vertical velocity contours from the numerics and the linear internal wave theory, respectively; coordinates are normalized by the sphere diameter, $2a$. Panels adapted from (*a*,*b*) Hanazaki et al. (2009a) and (*c*–*e*) Okino et al. (2017), with permission from Cambridge University Press.

axis. This force is directly proportional to the body volume $\mathcal{V}$, to the added-mass coefficient C_M, and hence to the drift volume $\mathcal{V}_D$, provided conditions mentioned in Section 2.2 are satisfied. With a stabilizing stratification ($\rho_z < 0$), it is directed upward, whatever the sign of V. Hence it behaves as a drag when the body settles but as a thrust when it rises. In the opposite limit, $Re \ll 1$, matched asymptotic expansions have been used to obtain the buoyancy-induced drag correction under various conditions. Neglecting diffusive effects (i.e., considering that the Péclet number, $Pe = PrRe$, is very large), Zvirin & Chadwick (1975) found the drag of a sphere settling in a linearly stratified fluid to increase by a factor of $1 + 1.06(Re/Fr^2)^{1/3}$ compared to the homogeneous case. Conversely, Candelier et al. (2014) examined the limit where Pe is small and found that the steady state drag increases by a factor of $1 + 0.66(Re/Fr)^{1/2}Pr^{1/4}$. Considering the Oseen regime, $0 < Re \ll 1$, Mehaddi et al. (2018) established that Candelier et al.'s correction applies if the ratio of the stratification characteristic length, ℓ_s, to the Oseen length, $\ell_O = aRe^{-1}$, is much smaller than Pr^{-1}, whereas the former correction applies for $Pr^{-1} \ll \ell_s/\ell_O \ll Pr^{-1/4}$, and the classical inertial drag correction factor, $1 + \frac{3}{8}Re$, is recovered for $\ell_s/\ell_O \gg Pr^{-1/4}$. A different approach, suitable for computing the drag and the density distribution, was followed by Camassa et al. (2009, 2010). They used a Green's function formulation to express the effect of the density disturbance field at a given location via the Oseen tensor, eventually obtaining the force modification in the form of a volume integral over the whole domain. They applied this approach to spheres settling across a two-layer setup with a sharp pycnocline with height $h_p \ll a$. As **Figure 4a,b** shows, predictions closely follow the measured evolution of the displaced volume of light fluid and sphere speed. The entrained fluid column yields a reduction of the settling speed over a significant period of time and hence a prolonged residence time of the sphere near the interface.
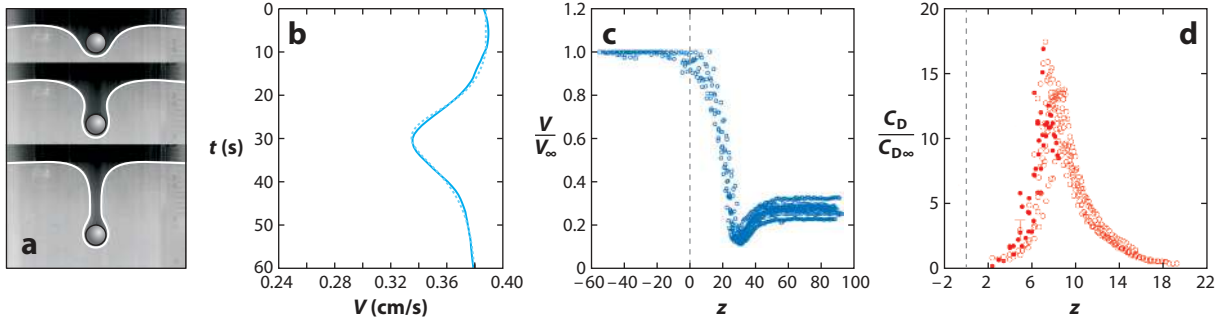
Figure 4

A sphere settling in a two-layer stratified fluid. (*a*) The entrained volume marked with dye, and (*b*) the sphere velocity versus time under Stokes flow conditions. (*c,d*) Normalized settling velocity (*c*) and drag coefficient (*d*) versus the distance z (in sphere diameters) to the top of the interface (*dashed line*); normalization is based on reference values V_∞ and $C_{D\infty}$ in a homogeneous fluid with a density equal to the local density at z in the two-layer setup. Panels adapted from (*a,b*) Camassa et al. (2010) and (*c,d*) Srdić-Mitrović et al. (1999), with permission from Cambridge University Press.

Similar but quantitatively more pronounced trends were reported with slightly negatively buoyant spheres crossing a thick pycnocline ($h_p \gg a$) in the parameter ranges of $0.7 \leq Re \leq 8$ and $6 \leq Fr \leq 20$ (Srdić-Mitrović et al. 1999). In this case, the drag coefficient, C_D, exceeds the reference value in the homogeneous top layer, $C_{D\infty}$, by more than one order of magnitude during some time (**Figure 4*d***). The settling speed starts decreasing as C_D departs from $C_{D\infty}$, and reaches a local minimum, V_m, still within the pycnocline but well after C_D has recovered its reference value (**Figure 4*c***).

Nearly spherical drops with $1 \lesssim Re \lesssim 10$ settling through a sharp pycnocline ($0.1 \leq h_p/a \leq 5$) were considered by Blanchette & Shapiro (2012), assuming the same viscosity in the drop and the carrying fluid. With a uniform drop–outer fluid interfacial tension, this configuration is close to that explored by Srdić-Mitrović et al. (1999) with solid spheres, yielding qualitatively similar evolutions of the settling velocity. However, the outer fluid can slip at the drop surface. Compared to a solid sphere, this tangential motion reduces the amount of fluid dragged down by the body, making the velocity minimum less pronounced, other things equal. Extra effects occur when the drop–outer fluid interfacial tension varies across the pycnocline, from γ_0 in the upper fluid to $\gamma_0 + \Delta\gamma$ in the lower one. With $\Delta\gamma < 0$, the Marangoni effect induces an additional traction directed upward, increasing the tangential velocity at the drop surface, thus reducing fluid entrainment. Thereby, instead of passing through a minimum, V can pass through a local maximum near the bottom of the pycnocline. Conversely, fluid entrainment is enhanced for $\Delta\gamma > 0$. The drop is then slowed down and may even remain trapped within the pycnocline for large-enough $\Delta\gamma$. The same mechanism takes place when surfactants accumulate at the drop–fluid interface. As they are advected to the back of the drop, where they lower the interfacial tension, the resulting Marangoni effect yields a downward traction, equivalent to a positive $\Delta\gamma$ (Martin & Blanchette 2017).

Situations in which V_m becomes negative have been reported with spheres settling at larger Reynolds numbers [$Re = \mathcal{O}(10^2)$], both in a two-layer setup with $h_p/a \ll 1$ (Abaid et al. 2004) and in a linear stratification (Doostmohammadi et al. 2014). The body then rises momentarily before settling again, which defines a so-called levitation regime. At first glance, the characteristics of this regime are reminiscent of the damped oscillations of bodies initially displaced from their neutrally buoyant position and subsequently allowed to oscillate freely. Predictions for these oscillations have been obtained by considering the drag to arise predominantly from either the radiation of

internal waves [drag $\propto V$ (Larsen 1969)] or usual frictional effects [drag $\propto V^2$ (Winant 1974)]. However, no neutrally buoyant position exists in the experiments reviewed above. Hence, no reversal of the settling speed, nor even a local minimum in its variation along the body path, can be explained without considering how the effective drag is altered by the distortion of isopycnals about the body.

Effects of this distortion on the near-field flow have been examined in simulations at low to moderate Re with $Pr = 700$. At the body surface, the fore–aft pressure difference and the frictional stress are enhanced compared to the unstratified case (Torres et al. 2000, Yick et al. 2009). In the near wake, the mechanism responsible for the downstream jet (Section 3.1) yields a secondary elongated vortex structure with opposite sign to the primary vortex ring resulting from the no-slip condition (Doostmohammadi et al. 2014). Empirical models have been developed for the corresponding drag modification, expressed through the normalized extra drag coefficient, $C_D/C_{D\infty} - 1$, that are based on the intuitive idea that the extra drag is just the buoyancy force corresponding to the volume of light fluid dragged by the body. At low Re, Yick et al. (2009) argued that this volume is essentially a spherical shell with dimensionless thickness $\delta_s/a \sim (Fr/Re)^{1/2}$ filled with light fluid dragged over a vertical distance $L_s/a \sim Fr^{1/2}$. This results in $C_D/C_{D\infty} - 1 \sim Re^{1/2}Fr^{-1}$, a scaling supported by Yick et al.'s direct determination of C_D but not by the relevant aforementioned low-Re asymptotic predictions. In the range $1 \lesssim Re \lesssim 10$, inspired by the classical definition of the drift volume (Section 2.2), Srdić-Mitrović et al. (1999) determined the contour of the dragged fluid column by marking the top plane $z = 0$ of the pycnocline with dye prior to the body release and subsequently tracked the dyed–undyed interface. By doing so, and by considering that the densities of the inner and outer fluids at depth z differ by $z\rho_z$, they directly estimated the extra buoyancy force due to the entrained column. For $Re \gtrsim 10$, experiments and simulations indicate that the extra drag on spheres and circular cylinders towed at constant speed scales as Fr^{-1} (Torres et al. 2000, Higginson et al. 2003, Hanazaki 2015), a trend supported by energetic considerations (Higginson et al. 2003). The above results have been used in empirical attempts aimed at estimating the stratification-induced drag from time records of the speed $V(t)$ of freely settling spheres (Srdić-Mitrović et al. 1999, Doostmohammadi et al. 2014). The basic idea is that the force balance customarily employed to predict the sphere motion in a homogeneous fluid, i.e., the ad hoc finite-Re extension of the Basset–Boussinesq–Oseen equation (Landau & Lifshitz 1987), may be applied to the stratified case by simply adding the depth-varying buoyancy force due to the undisturbed density gradient and the extra drag resulting from stratification effects [assumed to adjust instantaneously to the time variations of $V(t)$]. Srdić-Mitrović et al. (1999) found the extra drag predicted by this approach to agree well with their direct estimate of the extra buoyancy force associated with the entrained column (see **Figure 4d**).

Although these modeling attempts are appealing, they suffer from limitations that severely restrain their practical use. First, they are all based on high-Pr data. However, changes in the drag force have been shown to be significantly Pr-dependent, becoming weaker as Pr decreases, in line with the broadening of the downstream jet (Hanazaki et al. 2009b, Zhang et al. 2019). Second and even more serious, the definitions of the dragged volume used by the various authors differ from each other, so that no general predictive model exists. The reason for this was recently elucidated by performing a mathematical decomposition of the extra drag into density-induced and vorticity-induced contributions (Zhang et al. 2019). It was found that, for large Pr, most of the extra force in the ranges of $0.1 \lesssim Re \lesssim 100$ and $0.1 \lesssim Fr \lesssim 10$ is actually due to changes in the flow structure, such as those highlighted in **Figure 2a,b**, rather than to the extra buoyancy force associated with the dragged volume. It may also be noticed that effects of radiated internal waves are not accounted for in these models, although wave patterns have been identified downstream of the body as soon as Re is greater than approximately unity. However, their contribution to the

extra drag is expected to be small, becoming important only at very large Re for $Fr \simeq 1$ (Warren 1960, Scase & Dalziel 2004).

3.3. Anisotropic, Deformable, and Porous Bodies

The previous sections focused on spherical impervious bodies, by far the most documented case. However, effects of geometrical anisotropy, deformability, and porosity introduce important and often nonintuitive changes that have only begun to be explored.

The settling of anisotropic bodies, especially ellipsoids and disks, has been considered at moderate Reynolds number ($Re \lesssim 100$), under conditions where their motion in a homogeneous fluid reduces to a steady broadside-on fall. Although the background stratification is stabilizing for bodies released broadside-on, density disturbances acting on a slightly tilted oblate or prolate body settling in a stratified fluid may destabilize its initial orientation and make it eventually settle edge-on (Doostmohammadi & Ardekani 2014, Mrokowska 2018). The instability is rooted in the offset between the body axis and the location at which the upward jet emerges at the back of the body (**Figure 5a**). This offset results in a destabilizing torque that cannot be balanced by the restoring inertial torque when the ratio of inertia to stratification effects goes below a threshold. The transition takes place when stratification has reduced the settling velocity in such a way that
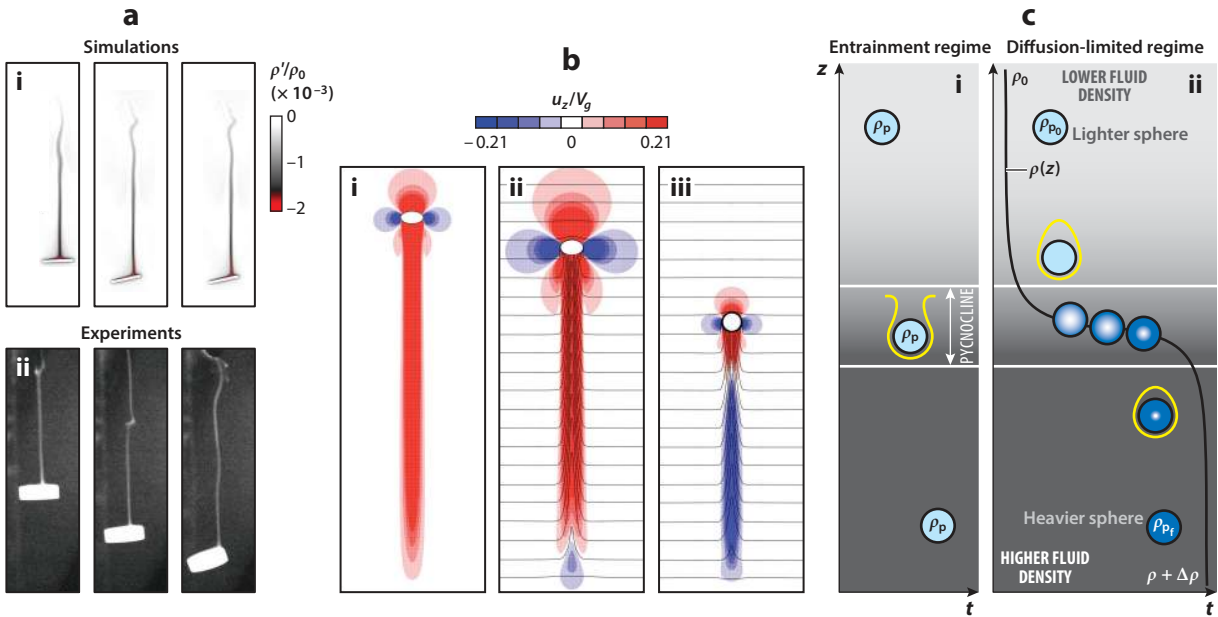
Figure 5

(*a*) Changes in orientation of a disk settling in a linearly stratified fluid from (*i*) simulations [with a Reynolds number (*Re*) of 60 and Froude number (*Fr*) of 3.4] and (*ii*) experiments ($Re = 90$, $Fr = 5$). (*b*) Effects of stratification on the shape of a rising drop of radius a and induced vertical velocity disturbance u_z with $Fr = \infty$ (*i*), 10.5 (*ii*) and 5.25 (*iii*), with $Re = 93$, a drop-to-fluid viscosity ratio of 1, and $We = \rho_0 V_g^2 a/\gamma_0 = 0.16$, where ρ_0 is the fluid reference density, V_g is the gravitational velocity, and γ_0 is the interfacial tension. The drop deformation reduces by 15% (30%) in between the first (last) two subpanels, with 3% (25%) difference in the rise speed. All scalings are based on V_g and a. (*c*) Schematic of the settling of a porous sphere in the entrainment regime (*i*) and the diffusion-limited regime (*ii*). Yellow lines indicate light fluid entrainment. Panels adapted from (*a*) Mercier et al. (2019); (*b*) Bayareh et al. (2013), with permission from American Institute of Physics; and (*c*) Kindler et al. (2010).

we have $V(t) \lesssim 4(\nu N)^{1/2}$, i.e., $V(t)/V_g \lesssim 4(ReFr)^{-1/2}$, with $V_g = (|\rho_s/\rho_0 - 1|ga)^{1/2}$, and ρ_s and a are the body density and radius, respectively (Mercier et al. 2019). At larger Reynolds numbers ($10^2 \lesssim Re \lesssim 10^3$), disks settling in a stratified fluid in the fluttering regime exhibit an increased horizontal dispersion and decreased fluttering amplitudes and inclination angles compared to the unstratified case (Lam et al. 2018).

Linear stratification reduces the deformation of rising drops (Bayareh et al. 2013). It does so through two different mechanisms illustrated by the two successive transitions between the three subpanels of **Figure 5b**. First, in inertial regimes, the intrinsic stratification-induced changes in the flow structure (Section 3.1) reduce the maximum tangential velocity at the drop surface for a given rise speed (Martin & Blanchette 2017). Second, as the local drop-to-fluid density contrast decreases during the drop ascent, the rise speed is reduced, decreasing inertia effects. Both effects lower the pressure difference between the front stagnation point and the drop's equator, reducing deformation.

The modeling of marine snow accumulation at pycnoclines (MacIntyre et al. 1995) motivated studies on the settling of porous spheres in a two-layer setup at low to moderate Re. Porous bodies that remain heavier than the denser fluid at any depth behave similarly to impervious bodies, defining an entrainment regime (**Figure 5c**, subpanel *i*). In contrast, the dynamics of highly porous bodies (with porosity $\phi_p \gtrsim 95\%$), having a solid matrix with density ρ_s, only slightly heavier than the denser fluid with density $\rho_0 + \Delta\rho$, are strongly impacted by stratification, since their actual local density is mostly controlled by the fluid they contain (Kindler et al. 2010). Once filled with the lighter fluid, such bodies have an effective density of $\rho_{p0} = (1 - \phi_p)\rho_s + \phi_p\rho_0$ and can be halted within the pycnocline if we have $(\rho_s - \rho_0)^{-1}\Delta\rho > 1 - \phi_p$. Diffusion of the denser fluid within the body is required to let it reach its final effective density, $\rho_{pf} = \rho_{p0} + \phi_p\Delta\rho$, and continue its settling. In this diffusion-limited regime (**Figure 5c**, subpanel *ii*), porous bodies experience enhanced retention times within the pycnocline, scaling as a^2 for spheres (Kindler et al. 2010). The diffusion mechanism generally combines with the entrainment effect due to the dragged fluid column (Section 3.2), which becomes dominant for small-enough bodies (Camassa et al. 2013). Experiments with real marine snow emphasize the crucial role of the density ratio $(\rho_s - \rho_0)^{-1}\Delta\rho$ in the body dynamics (Prairie et al. 2015). Numerical simulations with porous spheres confirm this role and reveal that the extra retention time increases logarithmically with the Péclet number, owing to the increased time required for the stratifying agent to diffuse through both the entrained fluid layer and the body (Panah et al. 2017).

# 4. BODIES CROSSING AN INTERFACE SEPARATING IMMISCIBLE FLUIDS

4.1. Critical Conditions for Breakthrough

Bodies translating due to a prescribed force (here gravity) perpendicular to an interface separating two immiscible fluids may or may not cross it, depending on the characteristics of their motion and on the fluid and body properties. If this motion is sufficiently slow, an approximate breakthrough condition is obtained by considering a static force balance and requiring that the body weight exceeds the sum of the capillary and buoyancy forces [see Vella (2015) and references therein].

For a sphere with density ρ_s, radius a, and volume $\mathcal{V}$, standing in the configuration depicted in **Figure 6**, static breakthrough takes place if we have

$$2\pi\gamma a \sin\psi \sin(\psi - \Phi) + g[\rho_1(\mathcal{V} - \mathcal{V}_{spc}) + \rho_2\mathcal{V}_{spc} + (\rho_2 - \rho_1)\mathcal{V}_{cyl}] < \rho_s\mathcal{V}g, \qquad 3.$$
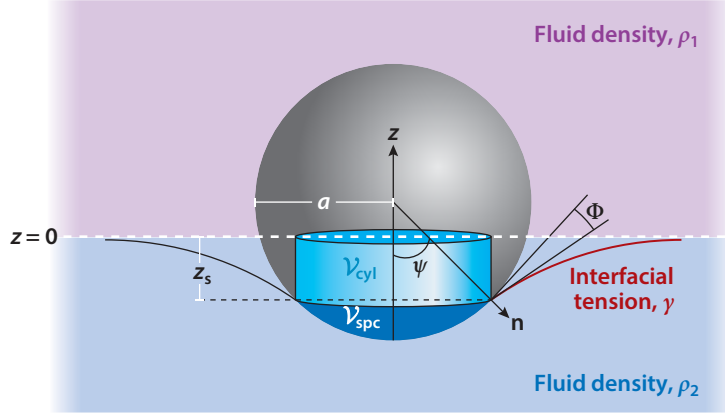
Figure 6

A sphere of radius a standing at the interface between two fluids of density ρ_1 and ρ_2 with interfacial tension γ, where **n** is the unit normal to the meniscus surface, Φ is the static pseudocontact angle, and ψ is the angular position of the pseudocontact line $z = -z_s$ at which the meniscus and the thin film standing in between the sphere and the interface match. In this configuration, static breakthrough takes place if the force balance Equation 3 holds. $\mathcal{V}_{cyl}$ and $\mathcal{V}_{spc}$ denote the volume of the pale blue cylinder and dark blue spherical cap, respectively. The film covering the bottom part of the sphere is not shown. Figure adapted from Pierson & Magnaudet (2018a), with permission from Cambridge University Press.

where ρ_1 (ρ_2) is the density of the upper (lower) fluid (hence $\rho_2 \geq \rho_1$), γ is the interfacial tension, Φ is the static pseudocontact angle, and ψ is the angular position of the pseudocontact line at which the meniscus and the thin film standing in between the sphere and the interface match. The first two contributions in the buoyancy force are those that would exist if there were no meniscus, $\mathcal{V}_{spc} = \frac{1}{3}\pi a^3 (2 - 3\cos\psi + \cos^3\psi)$ being the volume of the spherical cap located below the pseudocontact line (see **Figure 6**). The meniscus induces a shift between the position of the undisturbed interface, $z = 0$, and that of the peudocontact line, $z = -z_s$. As shown by Mansfield et al. (1997) and Keller (1998), this shift results in an additional buoyancy force proportional to the density difference $\rho_2 - \rho_1$ and the volume $\mathcal{V}_{cyl} = -\pi z_s (a \sin\psi)^2$ of the cylinder with height $-z_s$ standing on the pseudocontact line (see **Figure 6**). The force balance Equation 3 also applies to rising spheres, provided that g is negative (this convention is used throughout Section 4 for rising bodies). In that case, the stability of the fluid setup requires $\rho_2 \leq \rho_1$, so that the additional buoyancy force $(\rho_2 - \rho_1)g\mathcal{V}_{cyl}$ cooperates with the sphere weight and the capillary force to maintain the sphere in the denser fluid, while the usual buoyancy force, $g\{\rho_1(\mathcal{V} - \mathcal{V}_{spc}) + \rho_2\mathcal{V}_{spc}\}$, tends to drive it toward the lighter fluid.

To close Equation 3, one must know variations of the submergence $z_s^* = z_s/a$ with ψ, which requires one to determine the meniscus shape governed by the Young–Laplace equation, $(\rho_2 - \rho_1)gz = \gamma\nabla \cdot \mathbf{n}(z)$, where **n** is the unit normal to the meniscus surface.

This equation, supplemented with boundary conditions at the pseudocontact line and undisturbed interface, must in general be solved numerically (Huh & Scriven 1969, Rapacchietta & Neumann 1977). However, in the capillary-dominated regime, matched asymptotic expansions provide the closed-form expression $z_s^*(\psi) = \{\Gamma - \log 4 + \log\sqrt{Bo}\sin\psi \, [1 + \cos(\psi - \Phi)]\}\sin\psi$ $\sin(\psi - \Phi) + \mathcal{O}(Bo\log Bo)$, where $Bo = (\rho_2 - \rho_1)ga^2/\gamma$ is the Bond number and $\Gamma \simeq 0.577$ is the Euler constant (O'Brien 1996). The configuration maximizing the left-hand side of Equation 3 is then obtained with $\psi = \psi_{\max} \approx \pi/2 + \Phi/2$, so that breakthrough in the small-Bo limit is possible

for spheres with a relative body-to-fluid density contrast, $\beta = \frac{\rho_s - \rho_1}{\rho_2 - \rho_1}$, such that we have

$$\beta \geq \frac{3}{4}(1 + \cos \Phi)\left(Bo^{-1} - \frac{1}{4}\log Bo\right) + \mathcal{O}(1), \qquad\qquad 4.$$

where the neglected $\mathcal{O}(1)$ terms correspond to buoyancy effects that contribute to increase the critical density contrast. If ρ_2 and ρ_1 are approximately equal, these effects are negligible whatever the value of Bo, and Equation 4 may be approximated by the leading-order condition

$$Bo_s \gtrsim \frac{3}{4}(1 + \cos \Phi), \qquad\qquad 5.$$

with $Bo_s = (\rho_s - \rho_2)ga^2/\gamma$. The above solution for $z_s^*(\psi)$ only exists for $\psi \lesssim 3\pi/4$ (O'Brien 1996). Beyond this critical angle, the Young–Laplace equation does not have a solution so that no static equilibrium is possible. Consequently, the meniscus snaps if the pseudocontact line reaches such large angular positions. With finite buoyancy effects, a semiempirical model that assumes that the meniscus takes the form of an arc of a circle may be used to obtain a rough estimate of the minimum size allowing rigid spheres or spherical drops and bubbles to fall or rise across the interface (Maru et al. 1971, Bonhomme et al. 2012). Assuming that the Young–Laplace condition is satisfied at the pseudocontact line only and that the meniscus is tangent to both the sphere (assuming total wetting) and the undisturbed interface then yields $z_s^*(\psi) = -(2Bo)^{-1}\left\{-1 + [1 + 4Bo(1 - \cos\psi)]^{1/2}\right\}$. With large Bond numbers, buoyancy terms dominate in Equation 3, implying $\psi_{\max} \approx \pi - 2(2Bo)^{-1/4}$ and $z_s^* \approx -(2/Bo)^{1/2}$. Then Equation 3 yields the approximate breakthrough condition,

$$Bo_s \geq \frac{3}{2} + \mathcal{O}(Bo^{-3/2}), \qquad\qquad 6.$$

a crude criterion often used to estimate the minimum size of bubbles capable of crossing a liquid–liquid interface (Greene et al. 1988).

The influence of any initial motion is expected to modify the critical breakthrough condition. Incorporating dynamical effects in Equation 3 requires the time-dependent drag and inertia forces acting on the body to be known at any time. An attempt to model these forces in the inviscid limit was achieved by Lee & Kim (2008) to reproduce the behavior of small superhydrophobic spheres ($\Phi \approx 0$) impacting on water. Depending on their characteristics (ρ_s, a) and initial velocity V_i, such spheres may either float after having achieved damped oscillations, bounce off from the liquid, or sink after the meniscus has snapped. Scaling arguments revealed that bounds between the observed regimes correspond to constant values of the product $(\rho_s/\rho_2)^2 Bo^{3/2} We$, where $We = \rho_2 V_i^2 a/\gamma$ is the Weber number based on the impact velocity. Assuming the flow past the body to be potential and identical to that in an unbounded domain, one can compute the pressure distribution on the wetted part of the sphere, providing ψ-dependent expressions for the downward added-mass force and upward form drag. Adding these contributions to Equation 3, Lee & Kim (2008) could predict the early stages of the various observed evolutions. Besides capillary and buoyancy effects, the viscosity jump may also play a leading role in the body deceleration at the interface. When $\lambda = \mu_2/\mu_1$ is large, an additional effect arises when the body moves with a large Reynolds number, $Re_1 = \rho_1 V_1 a/\mu_1$, before the interface deforms. In that case, a wake has developed downstream and collapses when the body is virtually brought to rest as it starts deforming the interface (Pierson & Magnaudet 2018b). This situation is qualitatively similar to the sudden stop of a body in an unbounded fluid, in which case the wake collapse produces a thrust that lasts for some time after the stop. This thrust results in a history force on the body, like the Boussinesq–Basset force in the low-Re regime (Landau & Lifshitz 1987), but inertial by nature.

A theoretical prediction for this force was first obtained in the Oseen regime by Lovalenti & Brady (1993) for a sphere stopping in an unbounded fluid and then extended to larger Reynolds numbers by Lawrence & Mei (1995). At time t after the sphere has stopped, this force is $-\frac{3}{4}a(V_1t)^{-1}$ times the drag prior to the stop. In the present context of a semibounded domain, this prediction implies a reduction of the critical β for which the breakthrough occurs by a factor of $[1 + ka(V_1t)^{-1}]^{-1}$ with $k = \mathcal{O}(1)$, compared to the purely static estimates of Equations 4–6 (Pierson & Magnaudet 2018a).

## 4.2. Quasi-Static Detachment and Film Drainage

Spherical bodies that marginally satisfy Equation 3 cross the interface in a quasi-static manner. As the body gets close to the interface, a film forms ahead of it. This film is gradually drained, and the time it takes to rupture controls the breakthrough process, as is customary in liquid–liquid coalescence (Mohamed-Kassim & Longmire 2004). The characteristics of the film, as well as its drainage dynamics, depend dramatically on the nature of the body. Within the film that develops around a rigid sphere, the flow exhibits a Poiseuille profile or half-profile, depending on whether λ is large or small. In contrast, a plug-type profile takes place in the film that forms ahead of a gas bubble, provided λ is less than approximately unity (Debrégeas et al. 1998). In the former case, the film thickness decreases over time following a $t^{-1/2}$ law for $Bo \gtrsim 1$ (Hartland 1968, 1969; Jones & Wilson 1978) or a $t^{-1/4}$ law for $Bo \ll 1$ (Jones & Wilson 1978). In contrast, it decreases exponentially in front of a bubble close to a free surface for $Bo = \mathcal{O}(1)$ (Debrégeas et al. 1998, Pigeonneau & Sellier 2011). However, close to an interface with $\lambda = \mathcal{O}(1)$, this exponential behavior is quickly slowed down by the shearing motion that develops at the interface (Bonhomme et al. 2012). Around a rigid sphere or a nearly spherical drop with internal viscosity μ_s with $\lambda_s = \mu_s/\mu_1 \gg 1$, a constriction of the film surface (a so-called dimple) gradually develops within the subregion (corresponding to the location of the pseudocontact line in **Figure 6**) where the film matches with the meniscus (Hartland 1968, Jones & Wilson 1978, Chi & Leal 1989, Yiantsios & Davis 1990). The dimple makes the flow rate in the film uniform throughout the matching region, despite the acceleration resulting from the negative pressure gradient induced by the local variation of the capillary pressure. In the low-Bo limit, the drainage is first completed in the dimple region, so that the film is expected to rupture there. However, the breakthrough may also be achieved via the snapping mechanism mentioned in Section 4.1 if the submergence becomes large enough that the dimple position reaches the critical angle $\psi \approx 3\pi/4$. In that case, the body detaches from the interface before the drainage is completed, with the remaining film still stuck on its surface (Pierson & Magnaudet 2018b). Finite-Bo effects affect the drainage dynamics by modifying the angular variation of the film thickness. Smith & Van de Den (1984) showed that these effects make the film around a rigid sphere flatten in the region close to the axis (the bottom pole of the sphere in **Figure 6**). As time progresses, the thickness reaches a minimum there, causing the film to ultimately rupture at the pole well before it is totally drained. For bubbles and low-viscosity drops ($\lambda_s \lesssim 1$), no dimple forms at the edge of the film (Chi & Leal 1989). Film breakup then arises on the symmetry axis in a much shorter time than for a rigid sphere, other things equal. For such deformable bodies, another interfacial tension, γ_1, characterizing the drop–outer fluid interface, is involved, which yields a second Bond number, $Bo_1 = (\rho_s - \rho_1)ga^2/\gamma_1$. Increasing Bo and Bo_1 eases the deformability of the film boundaries, making the film thickness more uniform around the body front, thereby increasing the area of the small-gap region that needs to be drained for the breakthrough to happen. Hence, finite–Bond number effects slow down the drainage in this case (Pigeonneau & Sellier 2011, Bonhomme et al. 2012).

4.3. Tailing Regime

If the forces that drive the the body toward the second fluid, including possible inertial effects, significantly exceed those that tend to hold it at the interface, the breakthrough takes place before film drainage is completed. Then the body moves within the second fluid while its front part remains coated with a film of the first fluid and its rear part remains connected to the interface via a column of the same first fluid. In most cases, this column or tail lengthens as the body moves away from the interface until it pinches off at some point. Depending on the fluids properties, especially the viscosity and density contrasts and flow conditions prior to breakthrough, the tail may exhibit various geometries and dynamics (Maru et al. 1971; Dietrich et al. 2008, 2011; Bonhomme et al. 2012; Emery et al. 2018; Pierson & Magnaudet 2018a,b). The tailing configuration may take place under creeping flow conditions (Geller et al. 1986, De Folter et al. 2010, Jarvis et al. 2019). With a rigid sphere, the flow field is then completely characterized by three independent parameters, for instance, Bo, λ, and, for gravity/buoyancy-driven situations, the solid-to-fluid density contrast, β (Section 4.1). Under such conditions, the critical λ at which the film drainage/tailing transition takes place increases from $\lambda \approx 15$ for $Bo \approx 1$ to $\lambda \approx 50$ for $Bo \approx 5$ (Jarvis et al. 2019). Three additional characteristic parameters are required when drops and bubbles are involved, namely, λ_s, Bo_1 (Section 4.2), and a third Bond number, $Bo_2 = (\rho_s - \rho_2)ga^2/\gamma_2$, which is based on the drop–outer fluid interfacial tension γ_2 in the second carrying fluid. Moreover, two extra parameters come into play if flow inertia cannot be neglected: the fluid density ratio $\zeta = \rho_2/\rho_1$, which compares inertia effects in the two carrying fluids, and the Reynolds number characterizing the relative strength of inertia and viscous effects prior to breakthrough. For gravity/buoyancy-driven situations, this Reynolds number may be based on the gravitational velocity scale, $V_{g1} = \{(\rho_s/\rho_1 - 1)ga\}^{1/2}$, in which case it is frequently called the Archimedes number, $Ar_1 = \rho_1 V_{g1}a/\mu_1$. Therefore, inertial configurations are characterized by five and eight dimensionless parameters in the case of rigid and deformable bodies, respectively [for bubbles, λ_s is significantly less than unity and β is approximately equal to $(1 - \zeta)^{-1}$, which leaves six independent parameters]. The situation considered in Section 3 is recovered by setting the conditions $\lambda = \zeta = 1$, $Bo \to \infty$, and $\beta = -(\rho_s - \rho_1)/(a\rho_z)$ (with $Bo_1 = Bo_2$ for deformable drops and bubbles). In this case, $\beta^{1/2} = V_{g1}/(Na)$ is just the Froude number based on the Brunt–Väisälä frequency, $N_1 = (-g\rho_z/\rho_1)^{1/2}$ (with $\rho_z > 0$ for rising bodies, in line with **Figure 6**).

In a given fluid setup, the tail volume, and hence the fluid entrainment, increases with Ar_1 (**Figure 7a,b,g,h**). For a given Ar_1, the smaller Bo is, the larger the tail volume. This is because under quasi-static conditions, the initially flat interface deforms over a distance of the order of the capillary length, $l_c = [\gamma/(\rho_2 - \rho_1)g]^{1/2}$, i.e., $l_c/a = Bo^{-1/2}$, so that the deformation may extend over a larger region when Bo is small, yielding larger tail bases. As long as the body follows a rectilinear path prior to breakthrough, the tail preserves an axisymmetric geometry until pinch-off occurs, irrespective of the viscosity of the second fluid. For gravity/buoyancy-driven bodies in a homogeneous fluid, the onset of path instability takes place at a critical value, $Ar_1 = Ar_c$, which depends on the body shape (Ern et al. 2012), with $Ar_c = 55$ for a rigid sphere (Fabre et al. 2012). Consequently, three-dimensional tails are observed with spheres only for $Ar_1 > 55$ (Pierson & Magnaudet (2018a).

The corresponding threshold is significantly higher for gas bubbles, due to the different boundary condition at their surfaces, and greatly varies with their shape, i.e., with Bo_1. In particular, spherical-cap bubbles (encountered with $Bo_1 \gtrsim 10$ for $Ar_1 \gtrsim 1$) are not prone to path instability (Wegener & Parlange 1973), and no indication of a three-dimensional tail has been reported up to $Ar_1 \approx 500$ with such bubbles (Bonhomme et al. 2012).
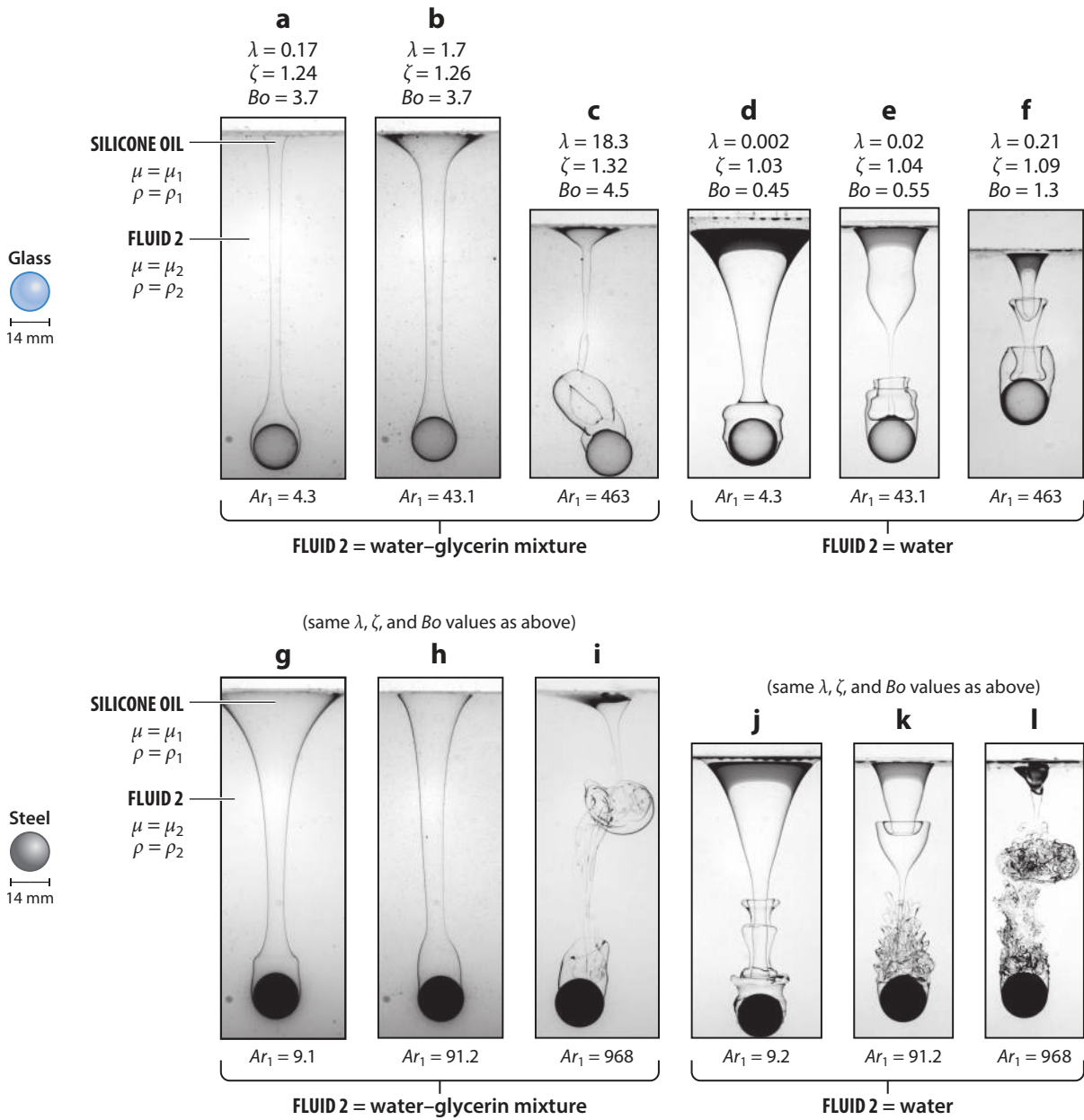
Figure 7

Tail geometries observed with 7-mm-radius spheres of (*a–f*) glass and (*g–l*) steel settling through various two-layer fluid setups. Abbreviations: Ar_1, Archimedes number in fluid 1; Bo, Bond number; ζ, density ratio of the two fluids (ρ_2/ρ_1); λ, viscosity ratio of the two fluids (μ_2/μ_1). Figure adapted from Pierson & Magnaudet (2018a), with permission from Cambridge University Press.

The relative magnitude of inertial and viscous effects in the second fluid may be quantified via a second Archimedes number, Ar_2, with $Ar_2 \approx Ar_1/\lambda$ for $\rho_2 \approx \rho_1$. With Ar_1 significantly higher than Ar_c but $Ar_2 \lesssim 1,500$, the tail geometry is reminiscent of the structure of transitional wakes past axisymmetric bodies, with well-defined hairpin-like regions (**Figure 7c,i**). In contrast, for $Ar_2 \gtrsim 1,500$, a specific instability develops along the tail surface, starting from the film that still coats the body and propagating downwards (**Figure 7d–f**). This instability results from the shear within the boundary layer that grows over time around the tail in the second fluid for $\lambda \ll 1$. In its early stage, its characteristics are consistent with those of inviscid Kelvin–Helmholtz modes (Pierson & Magnaudet 2018b), including the potentially stabilizing influence of capillary effects (Marmottant & Villermaux 2004). For $Ar_2 \gtrsim 2,500$, this instability eventually results in massive tail fragmentation, provided that the viscosity of the fluid within the tail is not too large, i.e., λ is not too small (**Figure 7j–l**). Indeed, viscous stresses within the tail dissipate a part of the energy supplied by the outer flow to the tail surface and, for a given Ar_2, are able to maintain the cohesion of the inner fluid if they are large enough. In the present context, fragmentation is driven by the shear provided by the boundary layer that surrounds the tail. This shear only depends on global flow scales (body velocity and local boundary layer thickness). This situation strongly differs from the classical turbulent picture (Villermaux 2007) in which the shear driving the fragmentation of a fluid element with a given size is a local quantity that depends on that size and on the dissipation rate. For this reason, the classical laws of turbulent breakup (Kolmogorov 1949, Hinze 1955) do not apply here. In particular, the characteristic mean radius of the droplets resulting from the fragmentation exhibits a weaker dependence with respect to γ and μ_1 than predicted by these laws (Pierson & Magnaudet 2018a).

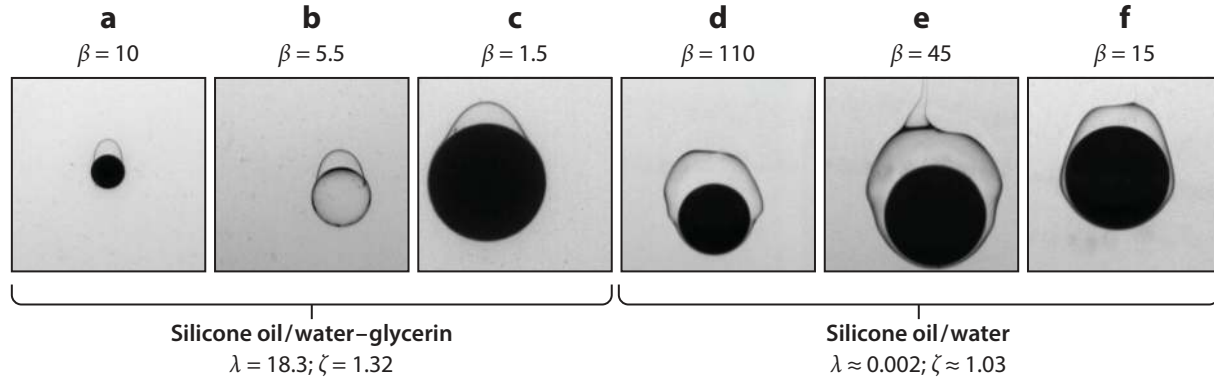## 4.4. Tail Pinch-Off and Beyond: Retraction Dynamics and Entrained Drops

With the exception of highly inertial situations where fragmentation occurs, the tail eventually pinches off after it has been continuously stretched over a distance usually much larger than the body size. Pinch-off may take place either very close to the base of the tail or much closer to the body than to the base. This process leaves a more or less long liquid thread attached to the body. When this thread is long enough, it may in turn undergo a capillary instability and discharge droplets at its tip in the surrounding fluid (Maru et al. 1971, Pierson & Magnaudet 2018b). Conversely, when it is short enough, it directly recedes toward the body and turns into a drop that remains stuck to its rear part (Pitois et al. 1999, Dietrich et al. 2008, Pierson & Magnaudet 2018a). The two distinct positions at which pinch-off may occur are reminiscent of the shallow seal and deep seal pinch-off types identified by Aristoff & Bush (2009) in cases where air cavities form after a hydrophobic sphere impacts a free surface (see also Truscott et al. 2014). However the dynamics of such air cavities and those of liquid tails exhibit two major differences. First, due to the negligible density of air compared to water, pressure is almost constant within a cavity. In contrast, both fluids have comparable densities in liquid–liquid systems, making the pressure vary along the tail axis, owing to hydrostatic and dynamic effects. Second, the outer flow almost obeys a shear-free condition at the cavity surface in the air–water system. Conversely, vorticity levels are large within at least one of the fluids in liquid–liquid systems, especially in the boundary layer around the tail for $\lambda \ll 1$. For these reasons, the tail pinch-off cannot be modeled via the free-surface potential flow approach suitable for cavity dynamics (Duclaux et al. 2007).

With $\zeta \approx 1$ and $Bo \gtrsim 1$, the body does not accelerate or decelerate much during the breakthrough if λ is of $\mathcal{O}(1)$. Under such conditions, shallow seal (deep seal) pinch-off is primarily governed by a balance between the capillary (buoyancy) pressure gradient along the tail and the radial acceleration of its surface. This yields characteristic pinch-off times of $\tau_\gamma \propto (\beta Bo)^{1/2}$ and

$\tau_g \propto \beta^{1/3}$, respectively, and the transition between the two pinch-off styles happens for $\tau_\gamma \approx \tau_g$, i.e., $Bo \approx \beta^{-1/3}$ (Pierson & Magnaudet 2018a). Only shallow (deep) pinch-off is possible at smaller (larger) Bo. In contrast, if λ is small (large), the body accelerates (decelerates) as it enters the second fluid. Strong decelerations are also encountered with low-density hydrophobic spheres impacting a free surface ($\zeta \gg 1$), and they reduce the pinch-off depth and the volume of the air bubble eventually entrained by the sphere (Aristoff et al. 2010). In liquid–liquid systems, time variations of the body velocity, $V(t)$, influence the pinch-off dynamics through inertia effects within the tail. Indeed, as far as the tail is pulled by the body, the cross-sectional averaged streamwise velocity of the inner fluid, $\langle W \rangle(z,t)$, is close to $V(t)$ near the body, implying that $\langle W \rangle \partial_z \langle W \rangle$ is close to the body acceleration, $\dot{V}(t)$, in that region. Hence, the longitudinal pressure gradient at the tail surface includes a dynamic contribution that increases from small values at the base of the tail to $-\rho_1 \dot{V}(t)$ at the rear of the body and that cooperates with the buoyancy contribution, $(\rho_2 - \rho_1)g$. The transition between the two types of pinch-off then depends on the parameter $\chi = -\{g(\zeta - 1)\}^{-1}\dot{V}$, which changes the pinch-off time τ_g into $\tau_g^* = \tau_g(1 + K\chi)^{-1/3}$, with $K = \mathcal{O}(1)$ (according to **Figure 6**, $\dot{V}$ is negative for an accelerating body). As a result, the transitional Bond number is reduced (increased) when the body accelerates (decelerates), which favors deep seal (shallow seal) pinch-off. Indeed, observations suggest that pinch-off essentially takes place close to the body for $\lambda \lesssim 0.1$.

The primary pinch-off splits the tail into two unequal ligaments that are no longer stretched. The longest of them recedes toward the body or the horizontal interface, depending on whether the pinch-off is of shallow or deep seal type. This ligament is then similar in essence to a preelongated viscous thread with initial length $\mathcal{L}_0$ and radius $\mathcal{R}_0$ receding in another viscous fluid, a configuration known to exhibit a rich phenomenology (Stone 1994). In general, the thread's fate is governed by the viscosity and density ratios; the thread aspect ratio, $\Gamma_0 = \mathcal{L}_0/\mathcal{R}_0$; and the Ohnesorge number, $Oh_{\mathcal{R}_0} = \mu_1(\rho_1\gamma\mathcal{R}_0)^{-1/2}$. Provided that Γ_0 is less than a critical value, $\Gamma_c(\lambda, \zeta, Oh)$, the thread recedes as a whole, while breaking into a series of droplets for larger aspect ratios, due to the so-called end-pinching instability. In the end-pinching instability, initiated by curvature variations in the transition region between the tip and the thread cylindrical body, a neck forms and shrinks there, eventually leading to breakup and the formation of a droplet at the tip (Stone et al. 1986, Stone & Leal 1989). This mechanism is repeating, yielding the formation of a succession of droplets with satellites and subsatellites between daughter drops (Tjahjadi et al. 1992). Under creeping flow conditions, Γ_c reaches a broad minimum in the range $1 \lesssim \lambda \lesssim 10$ (Stone et al. 1986), making tails in that range most prone to breakup. Computations (Notz & Basaran 2004) and experiments (Castrejón-Pita et al. 2012) with shear-free cylindrical threads indicate that Γ_c sharply increases with Oh for $\lambda = \zeta = 0$. In contrast, no prediction for $\Gamma_c(\lambda, \zeta, Oh)$ is currently available for arbitrary λ and ζ. Experimental and computational observations in the tailing regime for $0.2 \lesssim \lambda \leq 50$ are in line with the above phenomenology (Maru et al. 1971, Manga & Stone 1995, Pierson & Magnaudet 2018b), although some extra complexity frequently arises because the tail is often far from cylindrical and a second pinch-off may occur at its opposite end (driven by the slowest of the two pinch-off mechanisms). Quantitative agreement with the viscous linear instability theory (Tomotika 1935) is achieved with nearly cylindrical tails regarding the size of the primary daughter drops for $\lambda = \mathcal{O}(1)$, and the tip retraction speed is well predicted by the marginal stability criterion (Powers et al. 1998). With small λ, sufficiently short tails recede with a modified Taylor–Culick velocity, $V_{\text{tip}} \approx \{(\zeta - 1)g\mathcal{L}_0 + \gamma(\rho_1\mathcal{R}_0)^{-1}\}^{1/2}$, in which buoyancy and capillary effects cooperate (Pierson & Magnaudet 2018b). In contrast, long-enough tails still undergo an end-pinching instability.

The volume of the drop that remains attached to the body after the pinch-off and the possible subsequent end-pinching sequence is a quantity of primary importance in engineering

| a | b | c | d | e | f |
| $\beta = 10$ | $\beta = 5.5$ | $\beta = 1.5$ | $\beta = 110$ | $\beta = 45$ | $\beta = 15$ |

Silicone oil/water–glycerin
$\lambda = 18.3$; $\zeta = 1.32$

Silicone oil/water
$\lambda \approx 0.002$; $\zeta \approx 1.03$

Figure 8

Examples of entrained drops past spheres with various sizes and densities in two different fluid setups. Abbreviations: β, solid-to-fluid density contrast; ζ, density ratio of the two fluids (ρ_2/ρ_1); λ, viscosity ratio of the two fluids (μ_2/μ_1). Figure adapted from Pierson & Magnaudet (2018a), with permission from Cambridge University Press.

applications, especially coating processes and steel elaboration (Section 1). It greatly varies with the flow conditions and may under certain circumstances exceed the volume of the body itself (**Figure 8**).

This drop also directly affects the body's final velocity, as it increases its volume and modifies its shape and the boundary condition on a fraction of its surface. Under static conditions, the shape of pendant drops with a set volume is governed by the Young–Laplace problem. Solving this problem has revealed that the volume of the largest drop that can remain attached to a sphere under total wetting conditions scales as Bo^{-n_s}, with $n_s \approx 1.1$ (Shoukry et al. 1975). Partial wetting reduces this maximum volume, as it lowers the vertical component of the capillary force at the contact line (Smith & Van de Den 1985). When the body moves, effects of the viscosity ratio come into play: The drop–outer fluid interface virtually obeys a no-slip condition for $\lambda \ll 1$, while it behaves approximately as a shear-free surface if λ is large. If the drop is thin compared to the body's characteristic length, the shear acting on its outer surface induces an internal lubrication flow, which makes the drag of the body/drop aggregate increase compared to that of the body alone, provided that λ is not too large. For a sphere, this drag increase arises up to $\lambda = 4$ under creeping flow conditions (Johnson 1981). For larger λ, the coated part of the sphere nearly behaves like a bubble surface, therefore reducing the overall drag. With gravity/buoyancy-driven bodies, the volume of the drop that is ultimately entrained, $\mathcal{V}_d$, results from the complex interplay between the above static and dynamic effects, with the additional constraint that the drag force acting on the aggregate must balance its net weight, $\{(\rho_s - \rho_2)\mathcal{V} + (\rho_1 - \rho_2)\mathcal{V}_d\}g$. For this reason, the relative drop volume, $\mathcal{V}_d^* = \mathcal{V}_d/\mathcal{V}$, also depends on the body density through the ratio $(\rho_s - \rho_2)/(\rho_2 - \rho_1) = \beta - 1$. Hence, it generally depends at least on Bo, λ, and β. Experiments indicate that $\mathcal{V}_d^*$ is primarily a decreasing function of Bo under conditions such that $\beta \lesssim 20$, but the influence of λ and β is still present in most cases and makes the corresponding dependence weaker than in the static case. Conversely, when β is large, $\mathcal{V}_d^*$ becomes an increasing function of $Bo_s = (\beta - 1)Bo$ (also involved in Equations 5 and 6) (Pitois et al. 1999). Qualitative models based on overall force balances correctly predict these general trends (Pierson & Magnaudet 2018a), especially the linear increase of $\mathcal{V}_d^*$ versus Bo_s in the limit of large β and small λ (Chen et al. 2018). However, no complete model is available to date that quantitatively predicts $\mathcal{V}_d^*$ as a function of Bo, λ, and β.
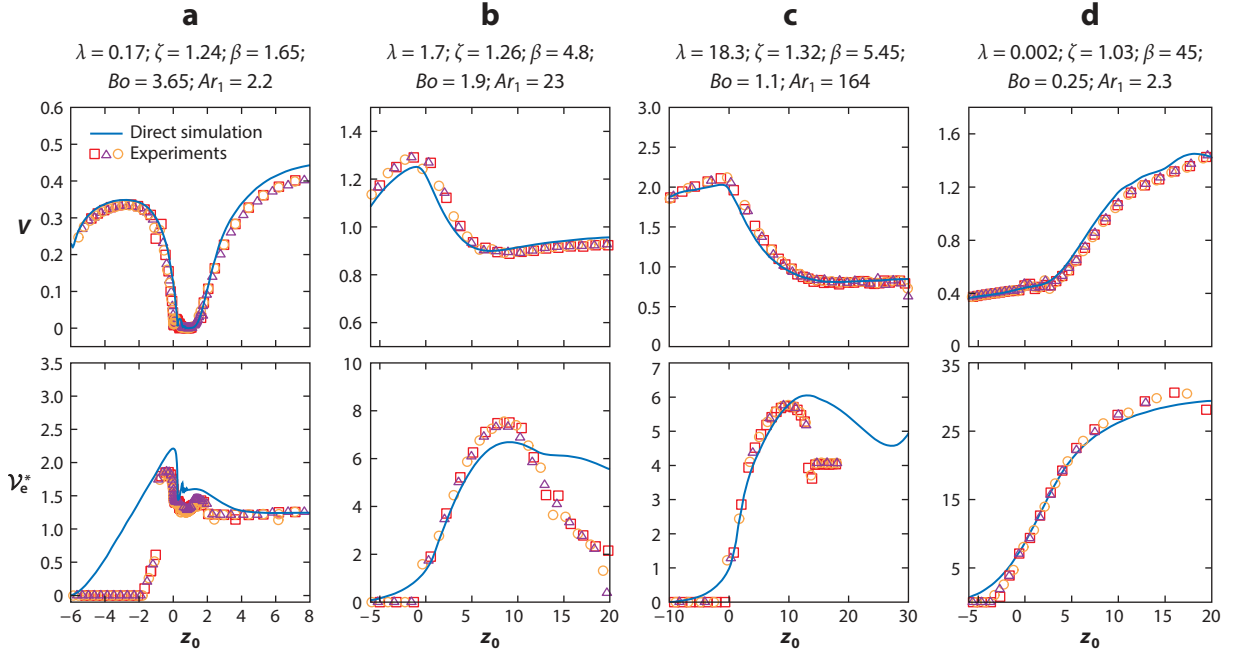
Figure 9

Two characteristics of interface breakthrough with a solid sphere, for increasing β: normalized settling velocity V (*top row*) and entrained volume $\mathcal{V}_e^*$ (*bottom row*) versus the distance z_0 (in sphere radii) from the sphere center to the horizontal interface. $\mathcal{V}_e^*$ is the fluid-and-sphere volume enclosed between the deformed interface and its initial position, $z = 0$. Limitations of the optical system gave erroneous estimates of $\mathcal{V}_e^*$ during some stages, especially in the presence of slight deflections of the horizontal interface. Abbreviations: Ar_1, Archimedes number in the upper fluid; β, solid-to-fluid density contrast; Bo, Bond number; ζ, density ratio of the two fluids (ρ_2/ρ_1); λ, viscosity ratio of the two fluids (μ_2/μ_1). Figure adapted from Pierson & Magnaudet (2018b), with permission from Cambridge University Press.

4.5. Evolution of Body Velocity and Entrained Volume During Breakthrough

The primary goal of every low-order model of hydrodynamic forces is to predict the body settling/rise velocity. However, it is challenging to derive such a model capable of dealing with a variety of breakthrough conditions, as the evolutions reported in **Figure 9** illustrate. In **Figure 9a**, a light sphere is stopped at the interface for a long time by capillary effects. Determining how long its release in the lower fluid takes requires an iterative process (Shah et al. 1972, Hashimoto & Kawano 1990) involving (*a*) a film drainage model to estimate the variation of the film thickness as a function of time for a given body's velocity and position, from which an updated pseudocontact angle $\psi(t)$ (**Figure 6**) is found; (*b*) an integration of the Young–Laplace equation to update the shape of the meniscus, and hence the submergence $z_s^*(t)$; (*c*) an integration of the force balance corresponding to the sum of the static forces in Equation 3 plus viscous drag and inertia forces, which provides the updated sphere velocity and position. Once the sphere settles in the lower fluid, a drop with relative volume $\mathcal{V}_d^* = \mathcal{V}_e^* - 1 \approx 0.2$ remains attached to its top (**Figure 9a**, bottom). Since the sphere is light ($\beta = 1.65$), the effective weight of the sphere-and-drop aggregate is only two thirds of that of the sphere alone. Hence, no realistic prediction of the final settling speed can be obtained without an accurate model for $\mathcal{V}_d^*$.

No sudden slowing down of the sphere near $z_0 = 0$ is noticed in **Figure 9b,d**, suggesting that capillary effects play a minor role in the breakthrough. In **Figure 9b**, where the primary pinch-off

is of deep seal type, $V(t)$ goes through a broad minimum just as $\mathcal{V}_e^*$ goes through its maximum. This indicates that the buoyancy force due to the tail (proportional to $\mathcal{V}_{cyl}$ in Equation 3) is responsible for the gradual slowing down of the sphere. Consequently, predicting this deceleration requires one to know the angular position $\psi(t)$ of the corresponding pseudocontact line, which amounts to determining the shape of the tail. Since the flow is inertial ($Ar_1 = 23$), this prediction can only be achieved through an extended version of the Young–Laplace equation taking into account inertial effects in both fluids through simplified models, such as the long-wave approximation for the flow within the tail (Eggers & Dupont 1994). In **Figure 9c**, buoyancy effects are still important ($\zeta = 1.32$), but most of the strong deceleration of the sphere results from the large viscosity ratio ($\lambda = 18.3$). Predicting $V(t)$ throughout the breakthrough then requires appropriate closure laws for the added-mass and viscous drag forces in a two-fluid medium, the properties of which change abruptly at the angular position $\psi(t)$, from (ρ_2, μ_2) on the front part of the sphere to (ρ_1, μ_1) on its rear part. Lee & Kim (2011) attempted to develop such a model in the case of a small sphere released from rest at a free surface, assuming the stress distribution on the wetted part of the body to be identical at any time to that in a Stokes flow past a sphere translating steadily in an unbounded fluid. Including the corresponding ψ-dependent viscous drag in Equation 3, Lee & Kim could reproduce the sphere descent and quantify the magnitude of the viscous resistance compared to static effects.

Without modeling dynamic effects during the breakthrough, one may obtain a realistic estimate of the final settling speed, V_2, at low cost, provided that (*a*) the attached drop is small enough to leave the drag coefficient and the sphere equatorial cross-section unchanged and (*b*) the initial and final flow regimes are similar in the sense that, in both of them, the drag coefficient exhibits the same Reynolds number dependence in the form of a power law with an exponent $-p$. Under such conditions, equating the drag force on the sphere-and-drop aggregate with its net weight in the initial and final configurations yields

$$\frac{V_2}{V_1} \approx \zeta^{\frac{p-1}{2-p}} \lambda^{\frac{-p}{2-p}} \left(\frac{\beta - 1 - \mathcal{V}_d^*}{\beta} \right)^{\frac{1}{2-p}}, \qquad\qquad 7.$$

where p equals 1 (creeping flow conditions) and V_2/V_1 is proportional to λ^{-1} and does not depend on the fluid density ratio. Conversely, p approaches zero if the Reynolds number is very large, in which case V_2/V_1 is independent of λ and varies as $[(\beta - 1 - \mathcal{V}_d^*)/(\beta\zeta)]^{1/2}$. In between these two limits, p is approximately 1/3 over a broad range of inertial conditions (Batchelor 1967), so that V_2/V_1 varies approximately as $(\zeta^2\lambda)^{-1/5}$ with the fluid properties. In **Figure 9c**, assuming p equals 1/3, Equation 7 predicts that V_2/V_1 is approximately equal to 0.45, which confirms the dominant role of ζ and λ in the sphere deceleration. In **Figure 9d**, buoyancy effects are weak ($\zeta = 1.03$) and the sphere's relative inertia is large ($\beta = 45$), so that the thick tail that develops as it settles and the large drop that remains stuck to its top (**Figure 8e**) have little effect on its dynamics. Hence, the sphere's acceleration is essentially driven by the huge viscosity jump ($\lambda = 0.002$). Predicting this acceleration throughout the breakthrough requires the same composite closure laws as in **Figure 9c**, but Equation 7, still with $p = 1/3$, correctly predicts V_2/V_1 to be approximately equal to 3.4.

Besides the body dynamics, the magnitude reached by the entrained volumes in **Figure 9**, together with the tail shapes in **Figure 7**, suggests that the entrainment process across an interface separating two immiscible fluids has little to do with the kinematic drift discussed in Section 2.2. Notably, in **Figure 9d**, which corresponds to $Ar_2 \gtrsim 10^3$, $\mathcal{V}_e^*$ reaches a maximum value close to 30, incommensurate with the drift volume $\mathcal{V}_D/\mathcal{V} = 1/2$ predicted by potential theory. Comparison with drift volumes predicted under Stokes or Oseen flow conditions (**Figure 1**) is not more
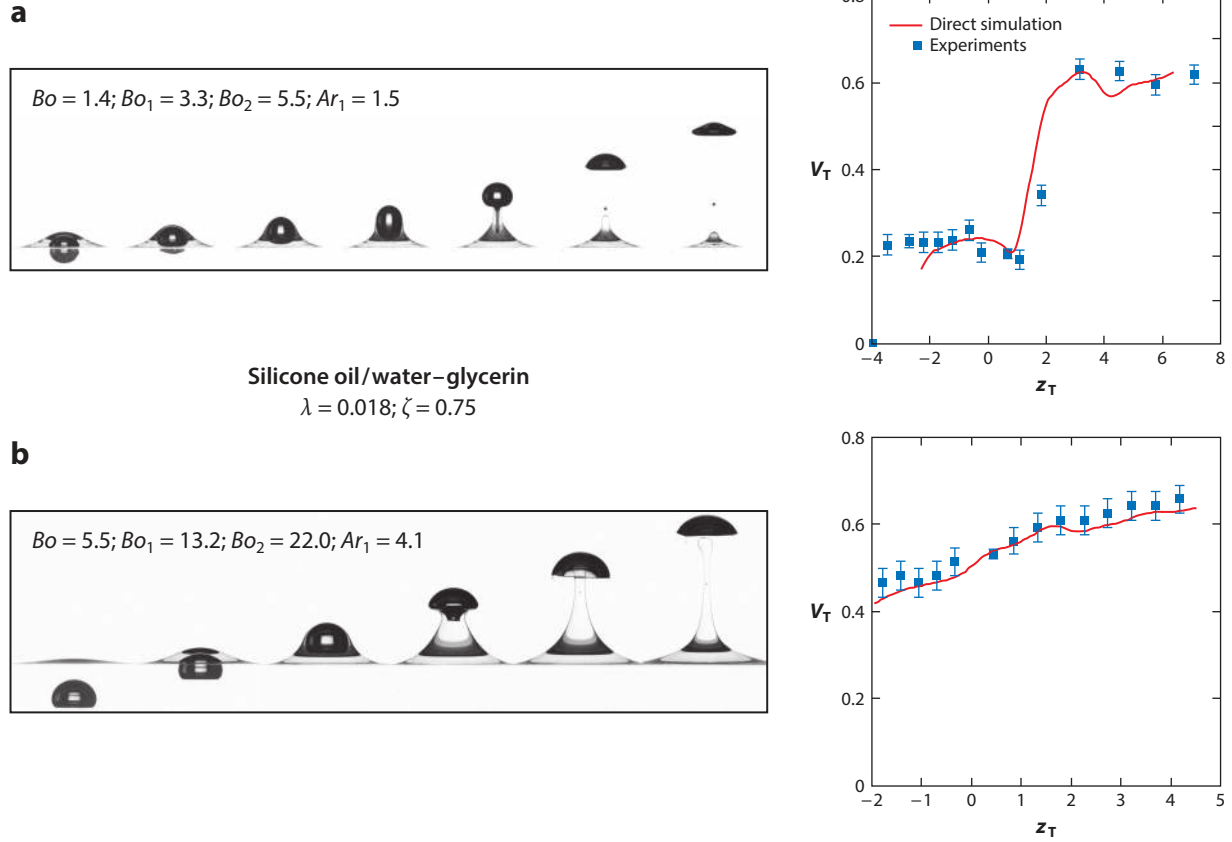
conclusive: Most of the drift volume arises from deflections of the marked plane at large radial distances from the sphere path in these situations, while deflections of the horizontal interface with immiscible fluids are always negligible beyond a few sphere radii. Without a doubt, vorticity generation at the body surface and through the three source terms specific to fluid inhomogeneities in Equation 1 is responsible for the actual characteristics of fluid entrainment in liquid tails past moving bodies. Due to the large bending of the interface at the base of the tail, each of these three terms is potentially large in that region, making vorticity generation locally intense under various conditions, as numerical simulations confirm (Pierson & Magnaudet 2018b). This conclusion is also supported by experiments in which a disk was towed across an oil–water interface and the shape of the corresponding tail was compared with potential flow predictions (Peters et al. 2016). Another experiment in which a bubble rose across a sharp density interface separating two liquids with negligible interfacial tension ($Ar_1 \gtrsim 1$ and $\zeta \approx 1$) revealed that $\mathcal{V}_e^*$ decreases with Ar_1 and with the density contrast $1 - \zeta$, which in particular points to the direct dependency of $\mathcal{V}_e^*$ on the Froude number, i.e., on β (Díaz-Damacillo et al. 2016).

4.6. Specificities of Deformable Drops and Bubbles

Drops and bubbles crossing an interface offer a greater variety of phenomena than rigid bodies owing to their deformability and to the internal shearing motion driven by the tangential stress condition at their surface. Their deformability in the first and second fluids is proportional to Bo_1 and Bo_2, respectively, whereas the ability of the inner fluid to move with respect to their surface is inversely proportional to λ_s. Hence the most significant differences with rigid bodies are found for large Bo_1 and Bo_2 and small λ_s, i.e., with large bubbles. The various regimes discussed in Sections 4.1–4.3 are successively encountered as the drop or bubble size (i.e., Bo) increases, all else being equal (Bonhomme et al. 2012, Emery et al. 2018): Drops that do not satisfy Equation 4 (with $\Phi = 0$) or Equation 6 remain trapped at the interface, possibly after a bouncing sequence (Feng et al. 2016, Singh et al. 2017), while slightly larger drops cross the interface in a quasi-static manner. Once released in the second fluid, they remain encapsulated in a thin shell corresponding to the remains of the film or meniscus left by the drainage process or the snapping mechanism. Larger drops or bubbles are only marginally affected by the resisting interfacial effects in Equation 3 and move away from the interface in the tailing mode. Pinch-off usually takes place as described in Section 4.4, and the resulting ligaments exhibit the same rich dynamics. However, with large-enough bubbles ($\lambda_s \approx 0, Ar_1 \gg 1$), tail pinch-off may be overtaken by film breakup at the bubble apex, which arises sooner (Uemura et al. 2010, Emery et al. 2018). In this case, the film first recedes along the bubble surface. The corresponding amount of liquid is collected at the tip of the entrained column, which subsequently undergoes an upward acceleration and penetrates into the bubble. If the Ohnesorge number $Ob_1 = \mu_1 (\rho_1 \gamma_1 a)^{-1/2} = Bo_1^{1/2}/Ar_1$ is small enough, concentric capillary ripples form at the bubble apex just after the film ruptures, and microdroplets are ejected from the receding film (Uemura et al. 2010).

Simulations have helped disentangle the influence of the various flow parameters in the inertia-less regime (Manga et al. 1993, Manga & Stone 1995) and in the $1 \lesssim Ar_1 \lesssim 10^2$ regime (Shopov & Minev 1992, Bonhomme et al. 2012, Singh & Bart 2015). When λ is large, the second fluid strongly resists interface deformation, which decelerates the drop. This in turn makes it flatten and become more oblate, which favors the formation of spherical-capped drops and bubbles. Conversely, drops passing from a higher- to a lower-viscosity fluid ($\lambda < 1$) accelerate and are stretched vertically throughout the breakthrough. The lower λ_s is, the larger the drop elongation is and the faster the drop rises or settles during the breakthrough, other things equal. Depending on Bo, Bo_1, and the shape and velocity of the drop by the time it gets close to the interface, two distinct deformation modes may develop. An elongating tail grows at the back of initially prolate drops with

a

$Bo = 1.4; Bo_1 = 3.3; Bo_2 = 5.5; Ar_1 = 1.5$

Silicone oil/water–glycerin
$\lambda = 0.018; \zeta = 0.75$

b

$Bo = 5.5; Bo_1 = 13.2; Bo_2 = 22.0; Ar_1 = 4.1$

Figure 10

Evolution of two bubbles passing from a higher- to a lower-viscosity fluid. The fluid setup consists of a silicone oil layer on top of a water–glycerin bath. (*a*) An initially nearly spherical bubble and (*b*) a spherical-capped bubble. The plots on the right show the evolution of the rise speed at the bubble apex, V_T [normalized by $(2ga)^{1/2}$] versus the distance z_T [in equivalent sphere diameters, $2a = (\frac{6}{\pi}\mathcal{V})^{1/3}$, with $\mathcal{V}$ the bubble volume] from the bubble apex to the horizontal interface. Abbreviations: Ar_1, Archimedes number in the lower fluid; Bo, interfacial Bond number; Bo_n, Bond number in fluid n; ζ, density ratio of the two fluids (ρ_2/ρ_1); λ, viscosity ratio of the two fluids (μ_2/μ_1). Figure adapted from Bonhomme et al. (2012), with permission from Cambridge University Press.

moderate to large Bo and Bo_1. It eventually breaks up, giving birth to secondary droplets, which move back to the interface due to the relaxation of the entrained liquid column and eventually co-alesce with their homophase (**Figure 10a**). Following this breakup, the drop relaxes toward a new equilibrium shape (possibly through an intermediate sequence of shape oscillations) controlled by the Bond and Archimedes numbers relevant in the second fluid, Bo_2 and Ar_2 ($Ar_2 = \frac{\zeta}{\lambda}Ar_1$ for bubbles). For initially oblate drops or bubbles with small to moderate Bo and Bo_1, an indentation forms at the back, which then turns into an annular tail that eventually recedes when the entrained liquid column relaxes toward the interface, following pinch-off or film rupture at the apex (**Figure 10b**).

Compared to rigid bodies, the settling or rise velocity of deformable drops and bubbles is more subtly influenced by density and viscosity jumps across the interface. This is due to the concomitant shape variations and distinct drag laws obeyed by drops or bubbles belonging to different shape families, as **Figure 10** illustrates. Owing to the much lower viscosity of the upper fluid, the initially nearly spherical bubble in **Figure 10a** experiences a sharp acceleration during the

breakthrough, tripling its rise speed within a distance of the order of twice its diameter. However, the drag coefficient of a spherical bubble rising with Reynolds number Re is $8/Re$ ($24/Re$) in the low- (high-) Reynolds number regime (Batchelor 1967), so that Equation 7 with $p = 1$ predicts that the bubble terminal velocity in the top fluid should be approximately 15 times larger than in the bottom fluid had the bubble kept a spherical shape. This erroneous estimate shows that the flattening of the bubble drastically mitigates the magnitude of the velocity jump. The rise velocity of the spherical-capped bubble in **Figure 10**b does not exhibit any jump during the breakthrough. Instead, it gradually increases and only experiences a 40% total variation. The rise velocity of spherical-capped bubbles is governed by the radius of curvature at the apex, $\mathcal{R}_a$, and varies as $(g\mathcal{R}_a)^{1/2}$ (Davies & Taylor 1950, Wegener & Parlange 1973). Hence, it is sensitive to the fluid viscosity and density only through their slight influence on $\mathcal{R}_a$.

SUMMARY POINTS

1. The flow around bodies settling (rising) in a fluid with a continuous vertical density profile exhibits three major characteristics: a distortion of isopycnals resulting in a column of light (heavy) fluid dragged by the body, a gradual squeeze of vertical scales as Fr decreases, and a baroclinically generated downstream jet that dominates the body dynamics at moderate to large Reynolds number.

2. In immiscible configurations, the salient characteristics of the inertial tailing regime are the position at which the tail pinches off, which is governed by the Bond number (possibly modified from effects of acceleration); the presence of boundary layers along the tail surface and their possible instabilities; and the fate of the liquid threads resulting from the primary pinch-off, especially the size of the drop that eventually sticks to the body. The viscosity contrast plays a key role in making rigid bodies accelerate or decelerate during the breakthrough, and in modifying the shape and velocity of drops and bubbles crossing an interface.

3. In all cases, the body dynamics are not solely controlled by the volume of the dragged fluid column, and in general, this volume cannot be estimated using classical predictions for the drift volume in a homogeneous fluid. The specific mechanisms by which vorticity is generated within the fluid and at interfaces modify the flow structure and cannot be ignored.

4. Internal (interfacial) waves are present in most cases in miscible (immiscible) configurations but do not play a discernible role in the body dynamics in the range of regimes considered here.

5. Thanks to advanced experimental and numerical tools, it is now possible to track the highly distorted interfaces and isopycnals involved in these flows and to obtain accurate estimates of entrained volumes and near-body velocity/vorticity distributions.

FUTURE ISSUES

1. The modeling of hydrodynamic loads related to density or viscosity inhomogeneities or jumps is still in its infancy. Attempts to account for the influence of the entrained column have been proposed in miscible stratified fluids, but they ignore the role of the modifications of the vorticity field, which has a direct and often dominant impact on

the drag. In the immiscible case, models coupling a simplified representation of the flow inside and outside the tail are required to determine its evolution up to the primary pinch-off and to estimate the tail fraction that eventually recedes toward the body surface and forms a drop. Models are also needed to properly estimate the viscous and inertial forces acting on the body while it is connected to the tail, since its rear and front parts are then immersed in two different fluids.

2. The nature and domain of existence of the instabilities that may affect the dragged column in the miscible and immiscible cases are far from clear and deserve specific investigations, not least because they have a direct impact on the body dynamics.

3. Available experiments and simulations have focused on bodies moving in a quiescent fluid, and very little is known on the combined effects of stratification and shear or strain. Fundamental investigations aimed at exploring these couplings are necessary and represent a compulsory step toward the understanding and prediction of stratification effects in the presence of a turbulent background.

4. This review has focused on the dynamics of isolated bodies. However, most situations of practical interest involve interacting particles, drops, or bubbles. Determining how these interactions are affected by the flow specificities at the particle scale and vice versa is still a largely unexplored area, although some pioneering work has been achieved in this direction, especially in estimating mixing properties.

DISCLOSURE STATEMENT

The authors are not aware of any biases that might be perceived as affecting the objectivity of this review.

ACKNOWLEDGMENTS

LITERATURE CITED

Abaid N, Adalsteinsson D, Agyapong A, McLaughlin RM. 2004. An internal splash: levitation of falling spheres in stratified fluids. *Phys. Fluids* 16:1567–80

Alldredge AL, Cowles TJ, MacIntyre S, Rines JEB, Donaghay PL, et al. 2002. Occurrence and mechanisms of formation of a dramatic thin layer of marine snow in a shallow Pacific fjord. *Mar. Ecol. Prog. Ser.* 233:1–12

Ardekani AM, Doostmohammadi A, Desai N. 2017. Transport of particles, drops, and small organisms in density stratified fluids. *Phys. Rev. Fluids* 2:100503

Ardekani AM, Stocker R. 2010. Stratlets: low Reynolds number point-force solutions in a stratified fluid. *Phys. Rev. Lett.* 105:084502

Aristoff JM, Bush JWM. 2009. Water entry of small hydrophobic spheres. *J. Fluid Mech.* 619:45–78

Aristoff JM, Truscott TT, Techet AH, Bush JWM. 2010. The water entry of decelerating spheres. *Phys. Fluids* 22:032102

Batchelor GK. 1967. *An Introduction to Fluid Dynamics*. Cambridge, UK: Cambridge Univ. Press

Bayareh M, Doostmohammadi A, Dabiri S, Ardekani AM. 2013. On the rising motion of a drop in stratified fluids. *Phys. Fluids* 25:103302

Bearon RN, Grünbaum D. 2006. Bioconvection in a stratified environment: experiments and theory. *Phys. Fluids* 18:127102

Bearon RN, Grünbaum D, Cattolico RA. 2006. Effects of salinity structure on swimming behavior and harmful algal bloom formation in *Heterosigma akashiwo*, a toxic raphidophyte. *Mar. Ecol. Prog. Ser.* 306:153–63

Benjamin TB. 1986. Note on added mass and drift. *J. Fluid Mech.* 169:251–56

Blanchette F. 2013. Mixing and convection driven by particles settling in temperature-stratified ambients. *Int. J. Heat Mass Transf.* 56:732–40

Blanchette F, Bush JWM. 2005. Particle concentration evolution and sedimentation-induced instabilities in a stably stratified environment. *Phys. Fluids* 17:073302

Blanchette F, Shapiro AM. 2012. Drops settling in sharp stratification with and without Marangoni effects. *Phys. Fluids* 24:042104

Bonhomme R, Magnaudet J, Duval F, Piar B. 2012. Inertial dynamics of air bubbles crossing a horizontal fluid–fluid interface. *J. Fluid Mech.* 707:405–43

Bush JWM, Thurber BA, Blanchette F. 2003. Particle clouds in homogeneous and stratified environments. *J. Fluid Mech.* 489:29–54

Camassa R, McLaughlin RM, Moore MNJ, Vaidya A. 2008. Brachistochrones in potential flow and the connection to Darwin's theorem. *Phys. Lett. A* 372:6742–49

Camassa R, Falcon C, Lin J, McLaughlin RM, Mykins N. 2010. A first-principle predictive theory for a sphere falling through sharply stratified fluid at low Reynolds number. *J. Fluid Mech.* 664:436–65

Camassa R, Falcon C, Lin J, McLaughlin RM, Parker R. 2009. Prolonged residence times for particles settling through stratified miscible fluids in the Stokes regime. *Phys. Fluids* 21:031702

Camassa R, Khatri S, McLaughlin RM, Prairie JC, White BL, Yu S. 2013. Retention and entrainment effects: experiments and theory for porous spheres settling in sharply stratified fluids. *Phys. Fluids* 25:081701

Candelier F, Mehaddi R, Vauquelin O. 2014. The history force on a small particle in a linearly stratified fluid. *J. Fluid Mech.* 749:184–200

Castrejón-Pita AA, Castrejón-Pita JR, Hutchings IM. 2012. Breakup of liquid filaments. *Phys. Rev. Lett.* 108:074506

Chemel C, Burns P. 2015. Pollutant dispersion in a developing valley cold-air pool. *Bound.-Layer Meteor.* 154:391–408

Chen H, Xu Q, Liang S, Li J. 2018. Film coating on a small sphere crossing an oil-water interface. *Phys. Rev. Fluids* 3:124003

Chi BK, Leal LG. 1989. A theoretical study of the motion of a viscous drop toward a fluid interface at low Reynolds number. *J. Fluid Mech.* 201:123–46

Chisholm NG, Khair AS. 2017. Drift volume in viscous flows. *Phys. Rev. Fluids* 2:064101

Condie SA, Bormans M. 1997. The influence of density stratification on particle settling, dispersion and population growth. *J. Theor. Biol.* 187:65–75

Cooray H, Cicuta P, Vella D. 2017. Floating and sinking of a pair of spheres at a liquid–fluid interface. *Langmuir* 33:1427–36

Dabiri JO. 2005. On the estimation of swimming and flying forces from wake measurements. *J. Theor. Biol.* 208:3519–32

Dabiri JO. 2006. Note on the induced Lagrangian drift and added-mass of a vortex. *J. Fluid Mech.* 557:105–13

Darwin C. 1953. Note on hydrodynamics. *Math. Proc. Camb. Philos. Soc.* 49:342–54

D'Asaro EA. 2003. Performance of autonomous Lagrangian floats. *J. Atmos. Ocean. Technol.* 20:896–911

Davies RM, Taylor GI. 1950. The mechanics of large bubbles rising through extended liquids and through liquids in tubes. *Proc. R. Soc. Lond. A* 200:375–90

De Folter JWJ, De Villeneuve VWA, Aarts DGAL, Lekkerkerker NHW. 2010. Rigid sphere transport through a colloidal gas–liquid interface. *New J. Phys.* 12:023013

Debrégeas G, De Gennes PG, Brochard-Wyart F. 1998. The life and death of 'bare' viscous bubbles. *Science* 279:1704–7

Denman KL, Gargett AE. 1995. Biological-physical interactions in the upper ocean: the role of vertical and small scale transport processes. *Annu. Rev. Fluid Mech.* 27:225–55

Díaz-Damacillo L, Ruiz-Angulo A, Zenit R. 2016. Drift by air bubbles crossing an interface of a stratified medium at moderate Reynolds number. *Int. J. Multiphase Flow* 85:258–66

Dietrich DE, Bowman MJ, Korotenko KA, Bowman MH. 2014. *Oil Spill Risk Management: Modeling Gulf of Mexico Circulation and Oil Dispersal*. Hoboken, NJ: Wiley

Dietrich N, Poncin S, Li HZ. 2011. Dynamical deformation of a flat liquid–liquid interface. *Exp. Fluids* 50:1293–303

Dietrich N, Poncin S, Pheulpin S, Li HZ. 2008. Passage of a bubble through a liquid-liquid interface. *AIChE J.* 54:594–600

Doostmohammadi A, Ardekani AM. 2014. Reorientation of elongated particles at density interfaces. *Phys. Rev. E* 90:033013

Doostmohammadi A, Dabiri S, Ardekani AM. 2014. A numerical study of the dynamics of a particle settling at moderate Reynolds numbers in a linearly stratified fluid. *J. Fluid Mech.* 570:5–32

Doostmohammadi A, Stocker R, Ardekani AM. 2012. Low-Reynolds-number swimming at pycnoclines. *PNAS* 109:3856–61

Duclaux V, Caillé F, Duez C, Ybert C, Bocquet L, Clanet C. 2007. Dynamics of transient cavities. *J. Fluid Mech.* 591:1–19

Eames I. 2003. The concept of drift and its application to multiphase and multibody problems. *Philos. Trans. R. Soc. Lond. A* 361:2951–65

Eames I, Belcher SE, Hunt JCR. 1994. Drift, partial drift and Darwin's proposition. *J. Fluid Mech.* 275:201–23

Eames I, Gobby D, Dalziel SB. 2003. Fluid displacement by Stokes flow past a spherical droplet. *J. Fluid Mech.* 485:67–85

Eames I, Hunt JCR. 1997. Inviscid flow around bodies moving in weak density gradients without buoyancy effects. *J. Fluid Mech.* 353:331–55

Eggers J, Dupont TF. 1994. Drop formation in a one-dimensional approximation of the Navier–Stokes equation. *J. Fluid Mech.* 262:205–21

Emery TS, Raghupathi PA, Kandlikar SG. 2018. Flow regimes and transition criteria during passage of bubbles through a liquid–liquid interface. *Langmuir* 34:6766–76

Ern P, Risso F, Fabre D, Magnaudet J. 2012. Wake-induced oscillatory paths of bodies freely rising or falling in fluids. *Annu. Rev. Fluid Mech.* 44:97–121

Fabre D, Tchoufag J, Magnaudet J. 2012. The steady oblique path of buoyancy-driven disks and spheres. *J. Fluid Mech.* 707:24–36

Feng J, Muradoglu M, Kim H, Ault JT, Stone HA. 2016. Dynamics of a bubble bouncing at a liquid/liquid/gas interface. *J. Fluid Mech.* 807:324–52

Geller AS, Lee SH, Leal LG. 1986. The creeping motion of a spherical particle normal to a deformable interface. *J. Fluid Mech.* 169:27–69

Greene GA, Chen JC, Conlin MT. 1988. Onset of entrainment between immiscible liquid layers due to rising gas bubbles. *Int. J. Heat Mass Transf.* 31:1309–17

Han Z, Holappa L. 2008. Mechanisms of iron entrainment into slag due to rising gas. *ISIJ Int.* 43:292–97

Hanazaki H. 2015. Numerical simulation of jets generated by a sphere moving vertically in a stratified fluid. *J. Fluid Mech.* 765:424–51

Hanazaki H, Kashimoto K, Okamura T. 2009a. Jets generated by a sphere moving vertically in a stratified fluid. *J. Fluid Mech.* 638:173–97

Hanazaki H, Konishi K, Okamura T. 2009b. Schmidt-number effects on the flow past a sphere moving vertically in a stratified diffusive fluid. *Phys. Fluids* 21:026602

Hartland S. 1968. The approach of a rigid sphere to a deformable liquid/liquid interface. *J. Colloid Interface Sci.* 26:383–94

Hartland S. 1969. The profile of the draining film between a rigid sphere and a deformable fluid-liquid interface. *J. Colloid Interface Sci.* 69:987–95

Hashimoto H, Kawano S. 1990. A study on encapsulated liquid- drop formation in liquid liquid gas systems: fundamental mechanism of encapsulated drop formation. *JSME Int. J. II* 33:729–35

Higginson RC, Dalziel SB, Linden PF. 2003. The drag on a vertically moving grid of bars in a linearly stratified fluid. *Exp. Fluids* 34:678–86

Hinze JO. 1955. Fundamentals of the hydrodynamic mechanism of splitting in dispersion processes. *AIChE J.* 1:289–95

Hokenson GJ. 1986. Vorticity with variable viscosity. *AIAA J.* 24:1039–40

Huh C, Scriven LE. 1969. Shapes of axisymmetric fluid interfaces of unbounded extent. *J. Colloid Interface Sci.* 30:323–37

Jacquemain D, ed. 2015. *Nuclear Power Reactor Core Melt Accidents*. Les Ulis, Fr.: EDP Sci.

Jarvis PA, Mader HM, Huppert HE, Cashman KV, Blundy JD. 2019. Experiments on the low-Reynolds-number settling of a sphere through a fluid interface. *Phys. Rev. Fluids* 4:024003

Johnson RE. 1981. Stokes flow past a sphere coated with a thin fluid film. *J. Fluid Mech.* 110:217–38

Jones AF, Wilson SDR. 1978. The film drainage problem in droplet coalescence. *J. Fluid Mech.* 87:263–88

Kawano S, Hashimoto H, Ihara A, Shin K. 1996. Sequential production of mm-sized spherical shells in liquid-liquid gas systems. *J. Fluids Eng.* 118:614–18

Keller JB. 1998. Surface tension force on a partly submerged body. *Phys. Fluids* 10:3009–10

Kindler K, Khalili A, Stocker R. 2010. Diffusion-limited retention of porous particles at density interfaces. *PNAS* 107:22163–68

King JA, Shair FH, Reible DD. 1987. The influence of atmospheric stability on pollutant transport by slope winds. *Atmos. Environ.* 21:53–59

Kobayashi S. 1993. lron droplet formation due to bubbles passing through molten iron/slag interface. *ISIJ Int.* 33:577–82

Kolmogorov AN. 1949. On the disintegration of drops in a turbulent flow. *Dokl. Akad. Nauk. SSSR* 66:825–28

Kumagai I, Davaille A, Kurita K. 2007. On the fate of thermally buoyant mantle plumes at density interfaces. *Earth Planet. Sci. Lett.* 254:180–93

Lam T, Vincent L, Kanso E. 2018. Passive flight in density-stratified fluids. *J. Fluid Mech.* 860:200–23

Landau LD, Lifshitz EM. 1987. *Fluid Mechanics*. Oxford: Pergamon. 2nd ed.

Lande R, Wood AM. 1987. Suspension times of particles in the upper ocean. *Deep-Sea Res.* 34:61–72

Larsen LH. 1969. Oscillations of a neutrally buoyant sphere in a stratified fluid. *Deep-Sea Res.* 16:587–603

Lawrence CJ, Mei R. 1995. Long-time behavior of the drag on a body in impulsive motion. *J. Fluid Mech.* 283:307–27

Lee DG, Kim HY. 2008. Impact of a superhydrophobic sphere onto water. *Langmuir* 24:142–45

Lee DG, Kim HY. 2011. Sinking of small sphere at low Reynolds number through interface. *Phys. Fluids* 23:072104

Levich VG, Krylov VS. 1969. Surface-tension-driven phenomena. *Annu. Rev. Fluid Mech.* 1:293–316

Lovalenti PM, Brady JF. 1993. The hydrodynamic force on a rigid particle undergoing arbitrary time-dependent motion at small Reynolds number. *J. Fluid Mech.* 256:561–605

MacIntyre S, Alldredge AL, Gotschalk CC. 1995. Accumulation of marine snow at density discontinuities in the water column. *Limnol. Oceanogr.* 40:449–68

Manga M, Stone HA. 1995. Low-Reynolds-number motion of bubbles, drops and rigid spheres through fluid–fluid interfaces. *J. Fluid Mech.* 287:279–98

Manga M, Stone HA, O'Connell RL. 1993. The interaction of plume heads with compositional discontinuities in the Earth's mantle. *J. Geophys. Res.* 98:19979–90

Mansfield EH, Sepangui HR, Eastwood EA. 1997. Equilibrium and mutual attraction or repulsion of objects supported by surface tension. *Philos. Trans. R. Soc. A* 355:869–919

Marmottant P, Villermaux E. 2004. On spray formation. *J. Fluid Mech.* 498:73–111

Martin DW, Blanchette F. 2017. Simulations of surfactant-laden drops rising in a density-stratified medium. *Phys. Rev. Fluids* 2:023602

Maru HC, Wasan DT, Kintner RC. 1971. Behavior of a rigid sphere at a liquid–liquid interface. *Chem. Eng. Sci.* 26:1615–28

Mehaddi R, Candelier F, Mehling B. 2018. Inertial drag on a sphere settling in a stratified fluid. *J. Fluid Mech.* 855:1074–87

Mercier MJ, Wang S, Péméja J, Ern P, Ardekani AM. 2019. Settling disks in a linearly stratified fluid. *J. Fluid Mech.* In press

Mohamed-Kassim Z, Longmire EK. 2004. Drop coalescence through a liquid/liquid interface. *Phys. Fluids* 16:2170–81

Mowbray DE, Rarity BSH. 1967. The internal wave pattern produced by a sphere moving vertically in a density stratified liquid. *J. Fluid Mech.* 30:489–95

Mrokowska MM. 2018. Stratification-induced reorientation of disk settling through ambient density transition. *Sci. Rep.* 8:412

Noh Y. 2000. Sedimentation of a particle cloud across a density interface. *Fluid Dyn. Res.* 27:129–42

Notz PK, Basaran OA. 2004. Dynamics and breakup of a contracting liquid filament. *J. Fluid Mech.* 512:223–56

O'Brien SBG. 1996. The meniscus near a small sphere and its relationship to line pinning of contact lines. *J. Colloid Interface Sci.* 183:51–56

Okino S, Akiyama S, Hanazaki H. 2017. Velocity distribution around a sphere descending in a linearly stratified fluid. *J. Fluid Mech.* 826:759–80

Panah M, Blanchette F, Khatri S. 2017. Simulations of a porous particle settling in a density-stratified ambient fluid *Phys. Rev. Fluids* 2:114303

Peters IR, Madonia M, Lohse D, Van Der Meer D. 2016. Volume entrained in the wake of a disc intruding into an oil-water interface. *Phys. Rev. Fluids* 1:033901

Pierson JL, Magnaudet J. 2018a. Inertial settling of a sphere through an interface. Part 1. From sphere flotation to wake fragmentation. *J. Fluid Mech.* 835:762–807

Pierson JL, Magnaudet J. 2018b. Inertial settling of a sphere through an interface. Part 2. Sphere and tail dynamics. *J. Fluid Mech.* 835:808–51

Pigeonneau F, Sellier A. 2011. Low-Reynolds number gravity-driven migration and deformation of bubbles near a free surface. *Phys. Fluids* 23:092102

Pitois O, Moucheront P, Weill C. 1999. Interface breakthrough and sphere coating. *C. R. Acad. Sci. Ser. IIB* 327:605–11

Poggi O, Minto R, Davenport WG. 1969. Mechanisms of metal entrapment in slags. *JOM* 21:40–45

Powers TR, Zhang D, Goldstein RE, Stone HA. 1998. Propagation of a topological transition: the Rayleigh instability. *Phys. Fluids* 10:1052–57

Prairie JC, Ziervogel K, Camassa R, McLaughlin RM, White BL et al. 2015. Delayed settling of marine snow: effects of density gradient and particle properties and implications for carbon cycling. *Mar. Chem.* 175:28–38

Rapacchietta AV, Neumann AW. 1977. Force and free-energy analyses of small particles at fluid interfaces. Part II. Spheres. *J. Colloid Interface Sci.* 59:555–67

Reiter G, Schwerdtfeger K. 1992. Observation of physical phenomena occurring during passage of bubbles through liquid/liquid interfaces. *ISIJ Int.* 32:50–56

Renggli CJ, Wiesmaier S, De Campos CP, Hess KU, Dingwell DB. 2015. Magma mixing induced by particle settling. *Contrib. Mineral. Petrol.* 171:96

Riebesell U. 1992. The formation of large marine snow and its sustained residence in surface waters. *Limnol. Oceanogr.* 37:63–67

Rydberg J, Cox M, Musikas C, Choppin GR, eds. 2004. *Solvent Extraction Principles and Practice*. New York: Marcel Dekker. 2nd ed.

Scase MM, Dalziel SB. 2004. Internal wave fields and drag generated by a translating body in a stratified fluid. *J. Fluid Mech.* 498:289–311

Sehgal RB, ed. 2012. *Nuclear Safety in Light Water Reactors*. Waltham, MA: Academic

Shah ST, Wasan DT, Kintner RC. 1972. Passage of a liquid drop through a liquid–liquid interface. *Chem. Eng. Sci.* 27:881–93

Singh KK, Bart HJ. 2015. Passage of a single bubble through a liquid–liquid interface. *Ind. Eng. Chem. Res.* 54:9478–93

Singh KK, Gebauer F, Bart HJ. 2017. Bouncing of a bubble at a liquid–liquid interface. *AIChE J.* 63:3150–57

Sinha A, Mollah AK, Hardt S, Ganguly R. 2013. Particle dynamics and separation at liquid–liquid interfaces. *Soft Matter* 9:5438–47

Shopov PJ, Minev PD. 1992. The unsteady motion of a bubble or drop towards a liquid-liquid interface. *J. Fluid Mech.* 235:123–41

Shoukry E, Hafez M, Hartland S. 1975. Separation of drops from wetted surfaces. *J. Colloid Interface Sci.* 53:261–70

Smith PG, Van de Den TGM. 1984. The effect of gravity on the drainage of a thin liquid film between a solid sphere and a liquid/fluid interface. *J. Colloid Interface Sci.* 100:456–64

Smith PG, Van de Den TGM. 1985. The separation of a liquid drop from a stationary solid sphere in a gravitational field. *J. Colloid Interface Sci.* 105:7–20

Sparks SRJ, Sigurdsson H, Wilson L. 1977. Magma mixing: a mechanism for triggering acid explosive eruptions. *Nature* 267:315–18

Srdić-Mitrović AN, Mohamed NA, Fernando HJS. 1999. Gravitational settling of particles through density interfaces. *J. Fluid Mech.* 381:175–98

Steinberger B, O'Connell RJ. 1998. Advection of plumes in mantle flow: implications for hotspot motion, mantle viscosity and plume distribution. *Geophys. J. Int.* 132:412–34

Stone HA. 1994. Dynamics of drop deformation and breakup in viscous fluids. *Annu. Rev. Fluid Mech.* 26:65–102

Stone HA, Bentley BJ, Leal LG. 1986. An experimental study of transient effects in the breakup of viscous drops. *J. Fluid Mech.* 173:131–58

Stone HA, Leal LG. 1989. Relaxation and breakup of an initially extended drop in an otherwise quiescent fluid. *J. Fluid Mech.* 198:399–427

Tjahjadi M, Stone HA, Ottino JM. 1992. Satellite and subsatellite formation in capillary breakup. *J. Fluid Mech.* 243:297–317

Tomotika S. 1935. On the instability of a cylindrical thread of a viscous liquid surrounded by another viscous fluid. *Proc. R. Soc. Lond. A* 150:322–37

Torres CR, Hanazaki H, Ochoa J, Castillo J, Van Woert M. 2000. Flow past a sphere moving vertically in a stratified diffusive fluid. *J. Fluid Mech.* 417:211–36

Truscott TT, Epps BP, Belden J. 2014. Water entry of projectiles. *Annu. Rev. Fluid Mech.* 46:355–78

Tsai SS, Wexler JS, Wan J, Stone HA. 2011. Conformal coating of particles in microchannels by magnetic forcing. *Appl. Phys. Lett.* 99:153509

Uemura T, Ueda Y, Iguchi M. 2010. Ripples on a rising bubble through an immiscible two-liquid interface generate numerous micro droplets. *EPL* 92:34004

Vella D. 2015. Floating versus sinking. *Annu. Rev. Fluid Mech.* 47:115–35

Villermaux E. 2007. Fragmentation. *Annu. Rev. Fluid Mech.* 39:419–46

Wagner GL, Young WR, Lauga E. 2014. Mixing by microorganisms in stratified fluids. *J. Mar. Res.* 72:47–72

Warren FWG. 1960. Wave resistance to vertical motion in a stratified fluid. *J. Fluid Mech.* 7:209–29

Wegener PP, Parlange JY. 1973. Spherical-cap bubbles. *Annu. Rev. Fluid Mech.* 5:79–100

Widder EA, Johnsen S, Bernstein SA, Case JF, Neilson DJ. 1999. Thin layers of bioluminescent copepods found at density discontinuities in the water column. *Mar. Biol.* 134:429–37

Winant CD. 1974. The descent of neutrally buoyant floats. *Deep-Sea Res.* 21:445–53

Yiantsios SG, Davis RH. 1990. On the buoyancy-driven motion of a drop towards a rigid surface or a deformable interface. *J. Fluid Mech.* 217:547–73

Yick KY, Torres CR, Peacock T, Stocker R. 2009. Enhanced drag of a sphere settling in a stratified fluid at small Reynolds numbers. *J. Fluid Mech.* 632:49–68

Zhang J, Mercier MJ, Magnaudet J. 2019. Core mechanisms of drag enhancement on bodies settling in a stratified fluid. *J. Fluid Mech.* In press

Zhang C, Churazov E, Schekochihin AA. 2018. Generation of internal waves by buoyant bubbles in galaxy clusters and heating of intracluster medium. *Mon. Not. R. Astron. Soc.* 478:4785–98

Zvirin Y, Chadwick RS. 1975. Settling of an axially symmetric body in a viscous stratified fluid. *Int. J. Multiphase Flow* 1:743–52